

Physics-based adaptivity of a spectral method for the Vlasov–Poisson equations based on the asymmetrically-weighted Hermite expansion in velocity space

Cecilia Pagliantini^{*}, Gian Luca Delzanno[†], and Stefano Markidis[‡]

Abstract

We propose a spectral method for the 1D-1V Vlasov–Poisson system where the discretization in velocity space is based on asymmetrically-weighted Hermite functions, dynamically adapted via a scaling α and shifting u of the velocity variable. Specifically, at each time instant an adaptivity criterion selects new values of α and u based on the numerical solution of the discrete Vlasov–Poisson system obtained at that time step. Once the new values of the Hermite parameters α and u are fixed, the Hermite expansion is updated and the discrete system is further evolved for the next time step. The procedure is applied iteratively over the desired temporal interval. The key aspects of the adaptive algorithm are: the map between approximation spaces associated with different values of the Hermite parameters that preserves total mass, momentum and energy; and the adaptivity criterion to update α and u based on physics considerations relating the Hermite parameters to the average velocity and temperature of each plasma species. For the discretization of the spatial coordinate, we rely on Fourier functions and use the implicit midpoint rule for time stepping. The resulting numerical method possesses intrinsically the property of fluid-kinetic coupling, where the low-order terms of the expansion are akin to the fluid moments of a macroscopic description of the plasma, while kinetic physics is retained by adding more spectral terms. Moreover, the scheme features conservation of total mass, momentum and energy associated in the discrete, for periodic boundary conditions. A set of numerical experiments confirms that the adaptive method outperforms the non-adaptive one in terms of accuracy and stability of the numerical solution.

Keywords. Vlasov–Poisson equations, spectral method, AW Hermite discretization, adaptive coefficients

1 Introduction

Many problems in plasma physics require the numerical solution of the kinetic Vlasov–Maxwell equations which describe microscopic physics via the seven-dimensional (three spatial and three velocity coordinates plus time) phase space density of the plasma. Important examples where the kinetic physics is essential include mechanisms of energy conversion in the Earth’s magnetosphere [20, 32], and in the solar corona [2], in the solar wind [3].

The Vlasov–Maxwell equations are challenging to solve numerically because of their high dimensionality, nonlinearities and large spatial and temporal scale separation. The latter already occurs at the microscopic level, due to the large difference in mass between electrons and ions, and becomes enormous when one compares microscopic scales with the characteristic scales of systems of interest. While the development of numerical methods for the solutions of the Vlasov–Maxwell equations is a very vibrant research area in its own right, the development of methods that accurately couple microscopic and macroscopic scales (i.e. the so-called fluid-kinetic coupling) remains a major challenge for computational plasma physics.

^{*}Corresponding author. Centre for Analysis, Scientific computing and Applications, Eindhoven University of Technology, 5600 MB Eindhoven, The Netherlands. Email: c.pagliantini@tue.nl

[†]T-5 “Applied Mathematics and Plasma Physics Group”, Los Alamos National Laboratory, Los Alamos, NM 87545, USA. Email: delzanno@lanl.gov

[‡]KTH Royal Institute of Technology, Stockholm, Sweden. Email: stefano.markidis@kth.se

In recent years there has been a renewed interest in the development of spectral methods for multi-scale plasma physics applications, owing in part to their interesting properties in terms of micro/macro coupling [8, 36]. These methods, also called transform methods, expand the plasma distribution function in suitable basis functions [14, 1, 17, 23, 19, 34, 4, 6, 11, 36, 30, 28, 26, 29, 5, 15, 31, 13, 24]. With a suitable spectral basis (i.e. an asymmetrically-weighted Hermite expansion or a Legendre expansion), the low-order moments of the expansion reproduce the macroscopic/large-scale behavior of the plasma while the kinetic physics can be captured by adding more moments only where and when necessary. Hence, spectral methods possess intrinsic fluid-kinetic coupling. Some recent plasma physics applications of spectral methods that were too computationally expensive for traditional methods can be found in [12, 33].

The majority of work on spectral methods for the Vlasov–Poisson problem to date has focused on spectral expansions based on Hermite functions in velocity space. Since the latter are naturally linked to Maxwellian distribution functions, this approach is well suited to capture the solution behavior of problems where the plasma distribution function remains nearly Maxwellian. Conversely, problems where the plasma develops a strong non-Maxwellian behavior might require an undesirably large number of expansion terms for convergence to an accurate solution. Schumer and Holloway [34] were the first to show that a suitable shifting and rescaling of the argument of the Hermite basis can significantly improve the convergence of the expansion. This was exploited by Camporeale et al. [8] to find eigenvalues of the linear stability problem of the Vlasov–Maxwell equations (for the Harris-sheet equilibrium configuration). The shift of the argument of the Hermite functions can be interpreted physically as centering the distribution function with the local mean flow for each plasma species. The rescaling of the argument of the Hermite functions can instead be related physically to the temperature or thermal velocity of each species. Since plasmas are characterized by complex dynamics and can develop strong plasma flows and/or heating/cooling locally, it is therefore natural to expect that adapting the argument of the Hermite basis functions to the local plasma conditions could considerably improve the convergence of the spectral expansion. For instance, a drifting Maxwellian distribution function with drift velocity u could be represented exactly with only one term in a Hermite expansion centered at u , while an expansion centered at $u_0 \neq u$ would require many more terms (more if $|u - u_0|$ is larger) for a given accuracy. However, the majority of existing time-dependent spectral approaches for plasma models that allow for shifting and rescaling coefficients of the Hermite expansion basis are limited to global constant coefficients, specified by the user at the beginning of the simulation, and are not adapted to the changing conditions in the simulations. In [24], the authors introduce a weighted Galerkin method with two separate scaling parameters for the Hermite polynomials that are fixed in time. More recently, in [16], the choice of the Hermite parameters is done via machine learning techniques but only for simple test cases and not for plasma applications.

To the best of our knowledge, the only existing spectral method for plasma physics that allows for the adaptivity of the Hermite expansion is an approach based on the regularized moment method called NRxx [4], together with its recent extension [38]. This method rewrites the Vlasov equation in a co-moving frame given by the local macroscopic velocity and scaled by the square root of the local temperature, with both quantities given by self-consistent, time-dependent, nonlinear partial differential equations, and discretizes it (in velocity) with *symmetrically weighted* Hermite functions.

In this paper, we consider a different approach which is much simpler from an algorithmic point of view and has different numerical properties. We expand the Vlasov equation with Hermite basis functions where the shifting u and rescaling α coefficients are constant. However, since u and α are related to the first and second moment of the distribution function, we monitor their time variation as we evolve the Vlasov equation numerically and when their change is bigger than a certain threshold, we perform a transformation from the old basis to a new basis obtained with the updated u and α . This transformation is performed *at a fixed instant of time*, which is crucial to avoid errors of order unity in the algorithm. This allows us to include the time adaptivity of the Hermite expansion in the algorithm without having to deal with a much more complex, nonlinear form of the Vlasov equation. Additionally, the properties of the numerical algorithm are also different from the NRxx method and its extension. We use *asymmetrically weighted* Hermite functions for the velocity direction, since their intrinsic property of fluid-kinetic coupling makes them an attractive method for micro/macro coupling problems. We use a Fourier discretization in physical space and an implicit time stepping technique and

demonstrate that the resulting numerical algorithm leads to the conservation of the discrete total mass, momentum, and energy (for periodic boundary conditions) of the system. Conversely, the NRxx method can only conserve the discrete total mass and momentum, while its recent extension can only conserve the discrete total mass and energy of the system. Finally, similar to the NRxx method and its extension, we use a physics-based criteria to adapt the u and α coefficients in time, exploiting the fact that they are related to the average velocity and temperature of each plasma species, i.e., the first and second moments of the plasma distribution function. However, while the physics-based choice is embedded in formulation of the NRxx method, in our case the prescription of how u and α change is flexible and one could envision other possibilities such as adopting a mathematically-based criteria based on some form of error minimization. Application of our new method to standard plasma physics test problems demonstrates the conservation properties of the algorithm and that the approach can indeed increase the accuracy of the simulations relative to a non-adaptive approach.

The paper is organized as follows. In Section 2, we introduce the model problem, which is governed by the system of Vlasov–Maxwell equations. In Section 3, we present the adaptive framework and the physically-based strategy that we use to adapt the Hermite parameters. In Section 4, we investigate the conservation properties of the adaptive fully discrete scheme and prove that it guarantees exact conservation of mass, momentum and energy. In Section 3.3, we provide implementation details, and we discuss the computational cost associated with updating the Hermite parameters. In Section 5, we explore the behavior of the adaptive fully discrete scheme on a number of manufactured solution tests and assess its performance on the two-stream instability. In Section 6, we offer our final remarks and conclusions.

2 Problem formulation

The focus of this work is on the electrostatic limit of the Vlasov–Poisson equations with the idea that a similar adaptive scheme can be designed *mutatis mutandis* for the general case of the Vlasov–Maxwell equations. The Vlasov–Poisson system describes the dynamics of a collisionless magnetized plasma under the action of the self-consistent electric field. We focus on a two species plasma consisting of electrons (labelled by “ e ”) and singly-charged ions (“ i ”), whose evolution at any time $t \in T \subset \mathbb{R}$ is described in terms of the distribution function $f^s(t, x, v)$ for the plasma species $s \in \{e, i\}$. Here, $x \in \Omega_x$ is the spatial coordinate and $v \in \Omega_v$ is the velocity coordinate. More in details, let the Cartesian phase space domain be denoted by $\Omega = \Omega_x \times \Omega_v \subset \mathbb{R}^2$ with $\Omega_x := [0, L]$, L being the length of the spatial domain, and $\Omega_v = \mathbb{R}$.

Let $L^2(\Omega)$ denote the standard Hilbert space of square integrable functions with inner product $(f, g)_\Omega := \int_\Omega f g dv dx$. We introduce the spaces of L^2 functions which are periodic in the spatial coordinate and tend asymptotically to zero at infinity in velocity space, namely

$$\begin{aligned} V &:= \{f(t, \cdot, \cdot) \in L^2(\Omega) : f > 0, f(t, 0, \cdot) = f(t, L, \cdot), f(t, \cdot, v) \rightarrow 0 \text{ as } |v| \rightarrow \infty\}, \\ W &:= \{g(t, \cdot) \in L^2(\Omega_x) : g(t, 0) = g(t, L)\}. \end{aligned}$$

The one-dimensional Vlasov–Poisson problem in $\Omega \times T$ reads: For $f_0^s \in V|_{t=0}$, find $f^s(t, x, v) \in C^1(T; L^2(\Omega)) \cap C^0(T; V)$, and $E(t, x) \in C^0(T; W)$ such that

$$\begin{cases} \partial_t f^s + v \partial_x f^s + \frac{q^s}{m^s} E \partial_v f^s = 0, & \text{in } T \times \Omega, \forall s, \\ \partial_x E = \sum_s q^s \int_{\Omega_v} f^s dv, & \text{in } T \times \Omega_x, \\ f^s(0, x, v) = f_0^s, & \text{in } \Omega, \end{cases} \quad (1)$$

where q^s and m^s denote the charge and mass of the species s , respectively.

We normalize the model equations as follows. Time t is normalized to the electron plasma frequency $\omega_{pe} = \sqrt{e^2 n_0^e / (\varepsilon_0 m^e)}$, where e is the elementary charge, m^e is the electron mass, ε_0 is the permittivity of vacuum, and n_0^e is a reference electron density. The velocity coordinate v is normalized to the electron thermal velocity $v_t = \sqrt{k T_e / m_e}$, where k is the Boltzmann constant and T_e is a reference electron

temperature; the spatial coordinate x is normalized to the electron Debye length $\lambda_D = \sqrt{\varepsilon_0 k T_e / (e^2 n_0^e)}$. We normalize the charge q_s and the mass m_s to the elementary charge e and the mass m^e , respectively. For simplicity, we keep the same symbols to denote dimensional and normalized quantities but in what follows we will focus on normalized quantities only.

We refer to the classic book of Glassey [18] for wellposedness results and the analysis of the Cauchy problem for the Vlasov–Poisson system.

2.1 Hermite–Fourier spectral discretization

For the numerical approximation of the Vlasov–Poisson problem (1), we pursue an Eulerian method of lines approach. We rely on the numerical scheme proposed in [11] by using spectral methods in phase space and the implicit midpoint rule as time-stepping. Observe that the adaptive method proposed in this work can accommodate other spatial and temporal discretizations. We summarize the main ideas of the numerical approximation in this subsection.

Let $\{\psi_n^{\alpha^s, u^s}\}_{n \in \mathbb{N}}$ be the family of generalized *asymmetrically weighted* (AW) Hermite functions,

$$\psi_n^{\alpha^s, u^s}(v) := (\pi 2^n n!)^{-1/2} H_n(\xi) e^{-\xi^2}, \quad \xi(v) := \frac{v - u^s}{\alpha^s}, \quad \alpha^s, u^s \in \mathbb{R}, \alpha^s > 0, \quad (2)$$

where H_n is the n -th Hermite polynomial, and α^s, u^s correspond to a scaling and a shift of the Hermite function, respectively. Concerning the spatial variable, let $\eta_k(x) := e^{\frac{2\pi i k}{L} x}$ denote the Fourier functions with wavenumber k . Since Ω_x is bounded, the set of Fourier functions $\{\eta_k(x)\}_{k \in \mathbb{Z}}$ form an orthonormal basis of $L^2(\Omega_x)$. The Hermite and Fourier functions satisfy the orthogonality relations

$$\int_{\mathbb{R}} \psi_n^{\alpha^s, u^s}(v) \psi_m^{\alpha^s, u^s}(v) \sqrt{\pi} (\alpha^s)^{-1} e^{\xi^2} dv = \delta_{n,m}, \quad \frac{1}{L} \int_{\Omega_x} \eta_k(x) \eta_h(x) dx = \delta_{k+h,0}, \quad (3)$$

for all $n, m \in \mathbb{N}$ and $h, k \in \mathbb{Z}$.

Let $N := (N_v, N_x) \in \mathbb{N} \times \mathbb{N}$, and let $\xi_j = \xi_j(v) := (v - u_j^s)/\alpha_j^s$ with $\alpha_j^s, u_j^s \in \mathbb{R}$. Based on the Fourier and Hermite functions, we define the finite dimensional approximation spaces

$$\begin{aligned} V_j^N &:= \text{span}(\{\psi_n^{\alpha_j^s, u_j^s}(v)\}_{n \in \Lambda_{N_v}}), & \widehat{V}_j^N &:= \text{span}(\{(\pi 2^n n!)^{-1/2} H_n(\xi_j)\}_{n \in \Lambda_{N_v}}), \\ W^N &:= \text{span}(\{\eta_k(x)\}_{k \in \Lambda_{N_x}}), \end{aligned} \quad (4)$$

where $\Lambda_{N_v} := \{n \in \mathbb{N} : 0 \leq n \leq N_v\}$, and $\Lambda_{N_x} := \{k \in \mathbb{Z} : -N_x \leq k \leq N_x\}$. Here \widehat{V}_j^N corresponds to the dual space of V_j^N .

Let T_h be a non-uniform partition of the temporal interval $T \subset \mathbb{R}$. Let us define the set of temporal indices as $\Lambda_{N_t} := \{j \in \mathbb{N} : 0 \leq j \leq N_t - 1, N_t \in \mathbb{N}\}$ so that $T_h = \bigcup_{j \in \Lambda_{N_t}} T_j$ where $T_j := [t^j, t^{j+1}]$. Let us denote with $\Delta t_j := |T_j|$ the local time step.

We pursue a Galerkin spectral discretization of (1), where we omit the superscript s for the sake of readability. The discretized problem in each time interval T_j , $j \in \Lambda_{N_t}$, reads: given the initial conditions $f_j^N(x, v) \in V_j^N \times W^N$ and $E_j^N(x) \in W^N$, find $(f_{j+1}^N(x, v), E_{j+1}^N(x)) \in (V_j^N \times W^N) \times W^N$ such that

$$\begin{cases} (f_{j+1}^N - f_j^N, h^N)_\Omega + \Delta t_j (v \partial_x f_{j+1/2}^N + \frac{q}{m} E_{j+1/2}^N \partial_v f_{j+1/2}^N, h^N)_\Omega = 0, \\ (\partial_x E_{j+1}^N, H^N)_{\Omega_x} = \sum_s q^s (f_{j+1}^{s,N}, H^N)_\Omega, \end{cases} \quad (5)$$

for all $h^N \in \widehat{V}_j^N \times W^N$ and $H^N \in W^N$, with $f_{j+1/2}^N := (f_{j+1}^N + f_j^N)/2$. In the interval T_j , the approximated functions f_j^N and E_j^N can be represented in their phase space spectral expansion in $V_j^N \times W^N$ and in W^N , respectively, as

$$\begin{aligned} f_j^N(x, v) &= \sum_{n \in \Lambda_{N_v}} \sum_{k \in \Lambda_{N_x}} \widehat{C}_{n,k}^j \psi_n^{\alpha_j, u_j}(v) \eta_k(x), \\ E_j^N(x) &= \sum_{k \in \Lambda_{N_x}} \widehat{E}_k^j \eta_k(x), \end{aligned} \quad (6)$$

where the linear functionals $\{\widehat{C}_{n,k}^j : V_j^N \times W^N \rightarrow \mathbb{C}\}_{n,k}$ and $\{\widehat{E}_k^j : W^N \rightarrow \mathbb{C}\}_k$ are the expansion coefficients defined as

$$\begin{aligned} (f_j^N \in V_j^N \times W^N) &\mapsto \left\{ \widehat{C}_{n,k}^j(f_j^N) := \int_{\Omega} f_j^N(x, v) \psi_n^{\alpha_j, u_j}(v) \eta_{-k}(x) \sqrt{\pi} \alpha_j^{-1} e^{\xi_j^2} dx dv, \right\}_{(n,k) \in \Lambda_{N_v} \times \Lambda_{N_x}}, \\ (E_j^N \in W^N) &\mapsto \left\{ \widehat{E}_k^j(E_j^N) := \int_{\Omega_x} E_j^N(x) \eta_{-k}(x) dx \right\}_{k \in \Lambda_{N_x}}, \end{aligned}$$

and, by construction, they form a basis for the dual spaces of $V_j^N \times W^N$ and of W^N , respectively.

By virtue of the orthogonality relations (3), the discrete problem (5) can be recast as a set of $N_t(N_v + 1)(N_x + 1)$ coupled algebraic equations in the unknown spectral coefficients. The resulting system reads: For each $j \in \Lambda_{N_t}$, given the initial spectral coefficients $\{\widehat{C}_{n,k}^j\}_{(n,k) \in \Lambda_{N_v} \times \Lambda_{N_x}}$ and $\{\widehat{E}_k^j\}_{k \in \Lambda_{N_x}}$, find $\{\widehat{C}_{n,k}^{j+1}\}_{(n,k) \in \Lambda_{N_v} \times \Lambda_{N_x}}$ such that,

$$\begin{cases} \frac{\widehat{C}_{n,k}^{j+1} - \widehat{C}_{n,k}^j}{\Delta t_j} + \sqrt{\frac{n}{2}} \frac{2\pi}{L} ik \alpha_j \widehat{C}_{n-1,k}^{j+1/2} + \frac{2\pi}{L} ik u_j \widehat{C}_{n,k}^{j+1/2} + \sqrt{\frac{n+1}{2}} \frac{2\pi}{L} ik \alpha_j \widehat{C}_{n+1,k}^{j+1/2} \\ \quad - \sqrt{2n} \frac{q}{m} \frac{1}{\alpha_j} \sum_{\ell \in \Lambda_{N_x}} \widehat{C}_{n-1,\ell}^{j+1/2} \widehat{E}_{k-\ell}^{j+1/2} = 0, \quad \forall (n, k) \in \Lambda_{N_v} \times \widehat{\Lambda}_{N_x}, \\ \frac{2\pi}{L} ik \widehat{E}_k^{j+1} - \sum_s q^s \alpha_j^s \widehat{C}_{0,k}^{s,j+1} = 0, \quad \forall k \in \widehat{\Lambda}_{N_x} \setminus \{0\}, \\ \widehat{E}_0^{j+1} = 0, \end{cases} \quad (7)$$

with $\widehat{\Lambda}_{N_x} := \{k \in \mathbb{Z} : 0 \leq k \leq N_x\}$. For the closure of the system of equations (7) we set $\widehat{C}_{n,k}^j = 0$, $j \in \Lambda_{N_t}$, whenever $n \notin \Lambda_{N_v}$ or $k \notin \Lambda_{N_x}$. When u_j and α_j have the same constant value for every $j \in N_t$, system (7) corresponds to the method studied in Refs. [36, 37, 6], where it was shown that such approach conserves total mass, momentum and energy in a finite time step.

2.2 Artificial collisional operator

The collisionless plasmas of interest here can develop smaller and smaller scales in velocity space as time evolves, a phenomenon called *filamentation*. The discretization of the velocity space is associated with a minimum wavelength that can be resolved to the extent that any simulation will inevitably run out of resolution. Closing system (7) with $\widehat{C}_{n,k}^j = 0$ for $n \notin \Lambda_{N_v}$ determines the finest resolution in velocity space. The filamentation is also associated with the well-known recurrence problem which is typical of higher-order Eulerian-Vlasov and spectral methods [10, 21, 9]. In order to mitigate the filamentation, it is customary to add a physical or artificial collisional term to the right hand side of the Vlasov equation. Specifically, the Vlasov equation with artificial collisions reads: Find $f^s \in C^1(T; L^2(\Omega)) \cap C^0(T; V)$, such that

$$\partial_t f^s + v \partial_x f^s + \frac{q}{m} E^N \partial_v f^s = \nu \mathcal{C}(f^s), \quad \text{in } \Omega \times T, \quad \forall s,$$

where ν is a positive bounded constant, and \mathcal{C} is the operator modeling the artificial collisionality.

We follow [7, Section 4] and consider the collisional operator defined, for any function $f_j^N \in V_j^N \times W^N$ and for all $(n, k) \in \Lambda_{N_v} \times \Lambda_{N_x}$, according to the discrete formulation (5), namely

$$(\mathcal{C}(f_j^N), \psi_n^{\alpha_j, u_j} \sqrt{\pi} e^{\xi_j^2} \eta_{-k})_{\Omega} = - \frac{n(n-1)(n-2)}{(N_v-1)(N_v-2)(N_v-3)} \widehat{C}_{n,k}^j. \quad (8)$$

This operator does not act directly on the first three modes of the Hermite expansion and, therefore, maintains the conservation laws of total mass, momentum and energy [7]. It corresponds to adding a reaction-advection-diffusion global operator in velocity space: indeed the term (8) can be obtained as a nonlinear combination of continuous terms involving the Lenard-Bernstein operator [25],

$$\mathcal{C}(f) = \partial_v \left(v f + \frac{1}{2} \partial_v f \right). \quad (9)$$

The function (9) is an instance of the Fokker-Planck form of the Landau collision operator $\mathcal{C}(f) := \partial_v(\mathbb{A}f + \partial_v(\mathbb{D}f))$, with the choices $\mathbb{A} = v - u$, $u = 0$ and $\mathbb{D} = T\mathbb{I}$, $T = 1/2$. With such choice the Lenard-Bernstein operator vanishes at the Maxwell-Boltzmann equilibrium $f = \pi^{-1/2}e^{v^2}$.

Additionally, it is known that the AW discretization of the Vlasov-Poisson system considered here can become numerically unstable (i.e. the L_2 norm of the distribution function is not bounded and can grow in time) [34]. This typically signals a lack of resolution such that the number of Hermite modes used in the simulation does not provide an adequate representation of the distribution function dynamics. The presence of a collisional operator adds numerical stability to the discretized equations, although in our experience the numerical instability is typically fixed by increased resolution. We remark that the techniques presented in this paper improve the numerical stability of the resulting algorithm since the dynamical adaptivity of the Hermite functions (by properly adjusting their shift and scaling argument) is intended to capture more accurately the dynamics of the distribution function. Indeed, the numerical experiments presented in Sec. 5 confirm the better numerical stability of the adaptive algorithm relative to an algorithm that does not use adaptivity.

Overall, we emphasize that, since the collisional term is a nondegenerate high order diffusion, it must always be used in a convergence sense (this is, in fact, the real meaning of the collisionless approximation [35]). In other words, the collisional coefficient ν has to be chosen in such a way that the problem remains consistent with the dynamics of collisionless plasmas of interest and, at the same time, introduces enough artificial viscosity to prevent the recurrence effect associated with the filamentation.

3 Dynamical adaptivity of the Hermite functions

The discretization in velocity space is a crucial aspect for the numerical treatment of kinetic models. Spectral approximations have the potential of yielding highly accurate solutions even in the presence of highly nonlinear dynamics. However, a poor choice of the basis functions might require spectral expansions with a large number of modes to achieve even moderate accuracy.

In order to illustrate this point, let us consider the case of a shifted Maxwellian distribution function

$$f = \exp\left(-\left(\frac{v - u_0}{\alpha_0}\right)^2\right), \quad (10)$$

with $u_0 \neq 0$ varied parametrically and $\alpha_0 = 1$. Let us try to represent f with an AW Hermite expansion centered at $u = 0$ and $\alpha = 1$, Eq. (6). We keep the total number of Hermite modes equal to 30. We represent the distribution function on 2000 points equally spaced point in velocity space between -2 and 5 and compute the relative error as the L_2 norm between the analytic and the expansion centered at $u = 0$. Figure 1 (left) shows the relative error as a function of u_0 . One can see that the error is practically zero and flat for $u_0 < 1$ but it starts to rise dramatically for $u_0 > 1$. For $u_0 = 2.4$ the error is $\sim 2\%$, while for $u_0 = 3$ the expansion solution is diverging with relative error $\sim 10^4$. Figure 1 (right) shows the analytic and the reconstructed distribution functions for the case $u_0 = 2.4$. One can notice that quite high oscillations begin to appear for $v < 2$, particularly where the analytic distribution function (10) is asymptotically going to zero. On the other hand, if we had centered the expansion with $u = u_0$, we would have captured the analytic function exactly with only one Hermite mode. This simple exercise illustrates nicely (1) how a significant departure in the shift of the argument of the Hermite functions inevitably leads to a strong lack of accuracy and, hence, (2) that centering the Hermite expansion appropriately is critical. In Section 5, we will show with numerical experiments this might lead to numerical instabilities when using an algorithm that does not adapt in time the shift and scaling of the Hermite functions.

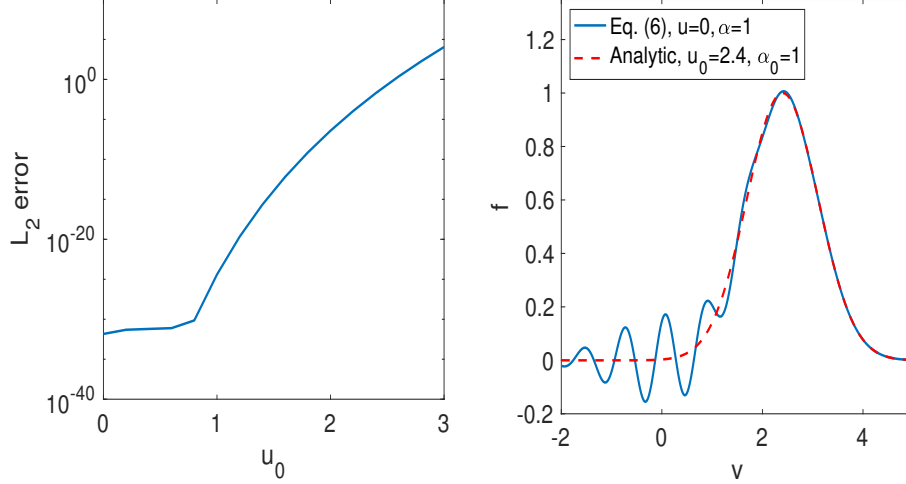


Figure 1: Relative error between the analytic distribution function given by Eq. (10) (u_0 variable and $\alpha_0 = 1$) and the distribution function given by expansion (6) with $u = 0$, $\alpha = 1$ and 30 Hermite modes as a function of u_0 (left); analytic and reconstructed distribution functions for $u_0 = 2.4$ ($\alpha_0 = 1$) (right).

We propose a numerical scheme where the discretization in velocity is adapted over time via a dynamical selection of the parameters α^s and u^s entering the Hermite basis functions (2). The gist of the proposed adaptive scheme is to update the Hermite basis functions at the beginning of each temporal interval by finding a spectral approximation able to “follow” the evolution of the numerical solution. Specifically, we allow the approximation space spanned by the Hermite polynomials to change between temporal intervals, at fixed time. If V_{j-1}^N is the approximation space in the interval $T_{j-1} = (t^{j-1}, t^j]$, we can select, at time t^j , new Hermite parameters so that in the following interval $T_j = (t^j, t^{j+1}]$ the discrete Vlasov–Poisson system is solved in the updated space V_j^N , which ideally has better approximation properties for a fixed number of Hermite modes N . See Figure 2 for a sketch of the adaptive algorithm.

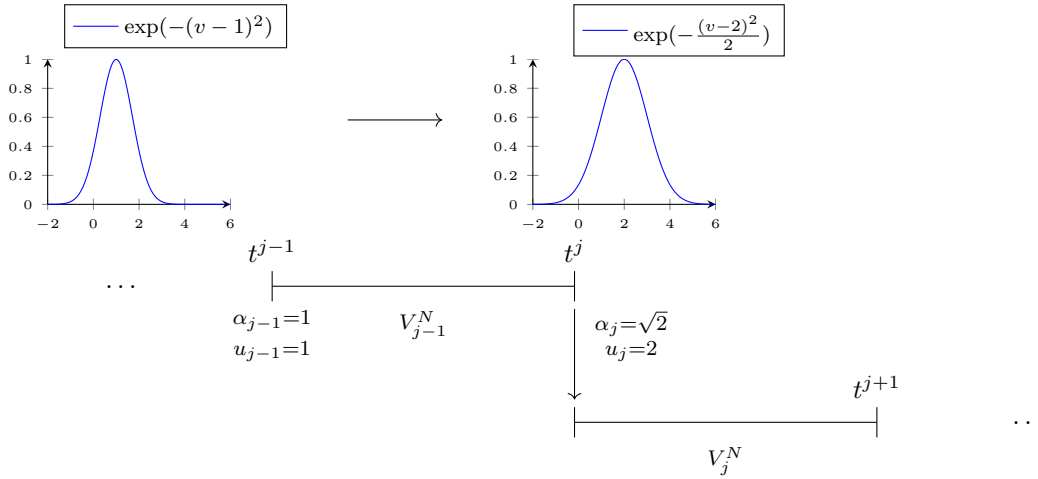


Figure 2: Sketch of the adaptive algorithm. Assume that, at time t^{j-1} , the distribution function is given by $f(v) = \exp(-(v-1)^2)$. The optimal Hermite parameters are then given by $(\alpha_{j-1}, u_{j-1}) = (1, 1)$. At time t^j new Hermite parameters (α_j, u_j) are computed to better approximate the current solution, here $f(v) = \exp(-(v-2)^2/2)$.

Moreover, in updating the approximation space, we need to map the numerical solution at time t^j into the updated space V_j^N in such a way that it can be a valid initial condition for the Vlasov–Poisson discrete problem posed in the interval T_j . This is a crucial aspect for the mathematical validity of the approximation. We observe that in the NRxx algorithm [4] this point is not discussed, while it is included in its recent extension [38].

Remark 3.1. A critical point in this adaptive approach is that we adapt the approximation space at fixed time. In other words, the discrete system in each time interval is always evolved with fixed parameters u and α , while these parameters can only change between time steps, i.e. at the interface between temporal intervals. Attempting to update the parameters during a time step might result in order-unity errors associated with mixing the two approximation spaces V_{j-1}^N and V_j^N at each fixed time t^j . Indeed, a spectral discretization relies on linear operations between the coefficients of the expansion of the distribution function with respect to the spectral basis, as shown in (7). Those operations are valid only if the spectral coefficients refer to the same basis. The reason is simply that a function expanded in two different bases produces different expansion coefficients even if the bases span the same space. Analogously, when changing the basis, the expansion coefficients need to be suitably re-computed.

Note that, in this paper, we consider only the time variation of u and α and leave to a future work the case where these parameters change both in space and time.

Two main ingredients are needed in the adaptive approach highlighted above: first, a criterion to update the Hermite parameters (α, u) , and second, a suitable definition of the operator \mathcal{P}_j^N mapping V_{j-1}^N into V_j^N . Let us start from the latter task.

3.1 Operator from V_{j-1}^N into V_j^N

Assume that at a given time t^j we have determined the “optimal” Hermite parameters (α_j, u_j) such that the adapted finite-dimensional velocity space is defined as $V_j^N := \text{span}(\{\psi_n^{\alpha_j, u_j}(v)\}_{n \in \Lambda_{N_v}})$. To evolve the discrete Vlasov–Poisson problem in the new space, we need to map the numerical solution f_j^N at time t^j from V_{j-1}^N to V_j^N . There are in principle many ways to define the operator mapping V_{j-1}^N into V_j^N . We chose to map f_j^N into its orthogonal projection onto V_j^N with respect to the L^2 -inner product weighted by ω_j .

Definition 1. Let V_{j-1}^N and V_j^N be the finite-dimensional spaces introduced in (4). We define $\mathcal{P}_j^N : V_{j-1}^N \subset L^2(\mathbb{R}) \rightarrow V_j^N \subset L^2(\mathbb{R})$ as the operator that maps any $f^N \in V_{j-1}^N$ into the function $\mathcal{P}_j^N f^N$ satisfying

$$(\sqrt{\omega_j}(\mathcal{P}_j^N f^N - f^N), \sqrt{\omega_j} h^N)_{\Omega_v} = 0, \quad \forall h^N \in V_j^N, \quad (11)$$

where $\omega_j = \sqrt{\pi} \alpha_j^{-1} e^{\xi_j^2}$ and $\xi_j = (v - u_j)/\alpha_j$.

The inner product in (11) is well-defined since $\sqrt{\omega_j} \mathcal{P}_j^N f^N \in L^2(\mathbb{R})$, and $\sqrt{\omega_j} h^N \in L^2(\mathbb{R})$. Moreover, since $f^N \in L^2(\mathbb{R})$ and $\{\psi_n^{\alpha_j, u_j}\}_{n \in \mathbb{N}}$ is a basis of $L^2(\mathbb{R})$, f^N admits a spectral expansion in $\{\psi_n^{\alpha_j, u_j}\}_{n \in \mathbb{N}}$, from which we can immediately see that also $\sqrt{\omega_j} f^N \in L^2(\mathbb{R})$.

In order to relate the spectral coefficients $\{\hat{C}_n(t^j, x)\}_{n \in \Lambda_{N_v}}$ of f^N to the spectral coefficients $\{\hat{P}_n(t^j, x)\}_{n \in \Lambda_{N_v}}$ of $\mathcal{P}_j^N f^N$ at time t^j , we derive the matrix representation of the linear mapping \mathcal{P}_j^N as follows. Owing to Definition 1, it holds

$$\hat{P}_n(t^j, x) = \sum_{m \in \Lambda_{N_v}} \hat{C}_m(t^j, x) (\sqrt{\omega_j} \psi_m^{\alpha_{j-1}, u_{j-1}}, \sqrt{\omega_j} \psi_n^{\alpha_j, u_j})_{\Omega_v} \quad \forall n \in \Lambda_{N_v}, \forall x \in \Omega_x. \quad (12)$$

Hence, the transformation matrix $\mathbb{P}^j \in \mathbb{R}^{(N_v+1) \times (N_v+1)}$ is defined, for all $n, m \in \Lambda_{N_v}$, as

$$\mathbb{P}_{n,m}^j = (\psi_m^{\alpha_{j-1}, u_{j-1}}, \psi_n^{\alpha_j, u_j})_{\Omega_v, \omega_j} := \int_{\Omega_v} \psi_m^{\alpha_{j-1}, u_{j-1}}(v) \psi_n^{\alpha_j, u_j}(v) \omega_j dv. \quad (13)$$

In order to give an explicit expression of the entries of \mathbb{P}^j we need to distinguish three different cases, associated with the change of only one parameter or both. Let us introduce the coefficients

$$a := \frac{\alpha_j}{\alpha_{j-1}} \in \mathbb{R} \setminus \{0\}, \quad b := \frac{u_j - u_{j-1}}{\alpha_{j-1}} \in \mathbb{R},$$

and let $K_{n,m} := 2^{\frac{m-n}{2}} (m!)^{-\frac{1}{2}} (n!)^{\frac{1}{2}} \in \mathbb{R}$ for all $n, m \in \Lambda_{N_v}$. Hence,

(i) If $\alpha_j \neq \alpha_{j-1}$ and $u_j \neq u_{j-1}$:

$$\mathbb{P}_{n,m}^j = K_{n,m} \frac{1}{a^{m+1}} \sum_{\substack{k=m \\ k-m \text{ even}}}^n \frac{1}{(n-k)! \left(\frac{k-m}{2}\right)!} \left(-\frac{2b}{a}\right)^{n-k} \left(\frac{1}{a^2} - 1\right)^{\frac{k-m}{2}}.$$

(ii) If $\alpha_j = \alpha_{j-1}$ and $u_j \neq u_{j-1}$:

$$\mathbb{P}_{n,m}^j = K_{n,m} \frac{1}{(n-m)!} (-2b)^{n-m}.$$

(iii) If $\alpha_j \neq \alpha_{j-1}$ and $u_j = u_{j-1}$:

$$\mathbb{P}_{n,m}^j = K_{n,m} \frac{1}{a^{m+1}} \frac{1}{\left(\frac{n-m}{2}\right)!} \left(\frac{1}{a^2} - 1\right)^{\frac{n-m}{2}}.$$

Note that, in all the above cases, if $n < m$ then $\mathbb{P}_{n,m}^j = 0$, namely the transformation matrix \mathbb{P}^j is lower triangular. By assuming $\alpha > 0$, the transformation matrix is invertible since it is lower triangular and all the diagonal elements are positive. Indeed $\mathbb{P}_{n,n}^j = a^{-(n+1)}$ for all $n \in \Lambda_{N_v}$.

The transformation matrix \mathbb{P}^j has been derived from the analytic calculation of the integrals (13) using the orthogonality properties of the Hermite polynomials together with the formula for the n -th Hermite polynomials [27, p. 255],

$$\begin{aligned} H_n(Ay + B) &= \sum_{k=0}^n \binom{n}{k} (2B)^{n-k} H_k(Ay) \\ &= \sum_{k=0}^n \binom{n}{k} (2B)^{n-k} \sum_{j=0}^{\lfloor k/2 \rfloor} A^{k-2j} (A^2 - 1)^j \binom{k}{2j} \frac{(2j)!}{j!} H_{k-2j}(y), \end{aligned}$$

valid for all $A \in \mathbb{R} \setminus \{0, 1\}$, $B \in \mathbb{R} \setminus \{0\}$.

3.2 Physics-based choice of the Hermite parameters α and u

The adaptivity criterion for the choice of the Hermite parameters should ideally minimize, at any given time t^j , the error between the numerical solution $f_j^N \in V_{j-1}^N$ and the exact solution $f^{\text{ex}}(t^j)$. Since the exact solution or an error indicator are in general not available, the adaptivity criterion for the selection of (α, u) remains one of the main challenges of an adaptive algorithm. We suggest here a criterion that is based on physics considerations.

At the initial time, the Hermite parameters (α_0, u_0) are chosen to minimize the projection error of the initial condition $f(t^0, x, v)$ onto the finite dimensional space associated with (α_0, u_0) for a fixed number of modes N . (Note that in the examples treated in section 5 we start from a Maxwellian plasma that can be described exactly with only one Hermite mode, hence the projection error is exactly zero.) For $t^j > 0$, one might envision a choice of the Hermite parameters driven by the minimization of the projection error of the approximate solution. However, this criterion does not ensure that $\|f^{\text{ex}}(t^j) - f_j^N\|$ is minimized, and, moreover, it “tends” to select as new Hermite parameters the (α, u) that are closest (in terms of Euclidean distance) to the old parameters.

By contrary, a physics-based choice aims at “correcting” the Hermite parameters according to the evolving dynamics. The idea of the physics-based adaptivity criterion that we propose is to select, at each time step, the shift parameter u as the average velocity of species s , and the scaling parameter α as the average thermal velocity. In particular, we set both quantities as the ratio of spatial averages of suitable physical quantities, see (14). The rationale for using the ratio of spatial averages is that we aim at capturing the amplitude and position of the Maxwellian reproducing the average behavior of the solution, rather than the oscillations associated with the deviation from a Maxwellian behavior.

Nevertheless, in the future we plan to extend the algorithm presented here to include spatially dependent quantities, i.e. $u(t, x)$ and $\alpha(t, x)$.

Let $f_j^N \in V_{j-1}^N \times W^N$ be the numerical solution of the discrete Vlasov–Poisson problem (5) at time t^j . We update the Hermite parameters as

$$\begin{aligned} u_j &= \frac{1}{n_j} \int_{\Omega} v f_j^N(x, v) dv dx, \quad \text{with } n_j := \int_{\Omega} f_j^N(x, v) dv dx \\ \alpha_j &= \sqrt{2} \sqrt{\frac{1}{n_j} \int_{\Omega} (v - u_j)^2 f_j^N(x, v) dv dx}. \end{aligned} \tag{14}$$

Using the spectral expansion (6) of f_j^N in $V_{j-1}^N \times W^N$ given by

$$f_j^N(x, v) = \sum_{n \in \Lambda_{N_v}} \sum_{k \in \Lambda_{N_x}} \widehat{C}_{n,k}^{j-1} \psi_n^{\alpha_{j-1}, u_{j-1}}(v) \eta_k(x),$$

the Hermite parameters in (14) can be efficiently derived using the relations

$$u_j = u_{j-1} + \frac{\alpha_{j-1}}{\sqrt{2}} \frac{\widehat{C}_{1,0}^{j-1}}{\widehat{C}_{0,0}^{j-1}}, \quad \alpha_j = \alpha_{j-1} \sqrt{1 + \sqrt{2} \frac{\widehat{C}_{2,0}^{j-1}}{\widehat{C}_{0,0}^{j-1}} - \left(\frac{\widehat{C}_{1,0}^{j-1}}{\widehat{C}_{0,0}^{j-1}} \right)^2}.$$

Since the physics-based definition of the Hermite parameters depends on the first two moments of the distribution function and on the kinetic energy, the fact that the AW scheme satisfies exactly the conservation laws of total mass, momentum and energy (which we anticipate here, for details see Section 4) is of fundamental importance. Moreover, since the spectral numerical discretization (5) is not generally positivity preserving (which in fact signals lack of resolution), the Hermite parameter α might become complex. In the numerical experiments of Section 5, the updated α_j is taken as the real part of (14).

Note that the Hermite parameters are not directly dependent on the value of the collisional term since the latter is constructed not to act on the first three modes of the Hermite expansion. However, since the evolution of the expansion coefficients depend on the collisional term, different choices of ν might yield a different evolution of the Hermite parameters.

3.3 Implementation and computational complexity of the adaptive algorithm

The adaptive pseudo-algorithm reads as follows.

Algorithm 1 Input: f_0^N , α_0 , u_0 , N_t

Initialize $E_0^N \in W^N$ via Eq. (7)
for $1 \leq j \leq N_t$ **do**
 Solve problem (5) in the interval T_{j-1} , with velocity approximation space V_{j-1}^N , to obtain $f_j^N \in V_{j-1}^N \times W^N$ and $E_j^N \in W^N$
 Compute the updated Hermite parameters α_j and u_j from f_j^N using (14)
 Compute $\mathcal{P}_j^N f_j^N \in V_j^N \times W^N$ using (11)
 Set $\mathcal{P}_j^N f_j^N$ as initial condition for the distribution function in the interval T_j
end for

In the non-adaptive strategy, system (7) is solved on a velocity approximation space V^N that does not change in time. Compared to the non-adaptive approach, the adaptive Algorithm 1 incurs an increased computational cost associated with updating the Hermite parameters, building the lower triangular matrix \mathbb{P} , and computing the spectral coefficients of the discrete distribution function projected into the updated approximation space. The construction of the transfer matrix \mathbb{P} requires one operation for each of the $(N_v)^2/2$ matrix entry; this is possible even in the case when both Hermite parameters are changing,

by computing the elements of \mathbb{P} in a suitable order. The computational complexity of the construction of \mathbb{P} is, therefore, $O(N_c^2)$, where N_c is defined as the number N_v of Hermite modes times the number of plasma species. Updating the expansion coefficients $P_{n,k} = \sum_{m \leq n} \mathbb{P}_{n,m} C_{m,k}$ for all $(n, k) \in \Lambda_{N_v} \times \Lambda_{N_x}$ requires $O(N_x N_c^2)$ operations every time the basis is updated. Despite this extra computational costs, the bulk of the computational effort during the simulation results presented here – for both non-adaptive and adaptive algorithms – is taken by the nonlinear solver.

We emphasize that the optimization and efficiency of our numerical MATLAB code is not the key point of this work, and we acknowledge that more efficient implementations are conceivable.

4 Conservation properties

One of the most important results of this paper is that the adaptive fully discrete scheme guarantees exact conservation of mass, momentum and energy. In order to prove this statement we proceed in two steps: first we show that, within each time interval, the conservation of mass, momentum and energy are satisfied; second we prove that the operator \mathcal{P}_j^N leaves the conserved quantities invariant. The first step of the proof boils down to show that the non-adaptive spectral method preserves the first three moments of the system and it is a well-known result in the spectral approximation of the Vlasov–Poisson and Vlasov–Maxwell equations using AW Hermite functions, see [11, Section 3]. Here we briefly summarize the main properties and derivations that will be used in the second step.

Let us define a *conserved quantity* \mathcal{M} as the function $\mathcal{M} \circ g : t \in T \mapsto \mathcal{M}(g(t)) \in \mathbb{R}$, such that $\mathcal{M} \circ g \in C^1(T)$ and satisfies

$$\frac{d\mathcal{M}(g(t))}{dt} = 0,$$

whenever $g(t) = f(t, \cdot, \cdot) \in L^2(\Omega)$ is the (weak) solution of the Vlasov–Poisson problem (1). As a first step, we need to show that the advancement in time preserves the conserved quantities of the continuous model: if $f_{j+1}^N \in V_j^N \times W^N$ is the numerical solution of the discrete problem (5) at time t^{j+1} , then the quantity $\mathcal{M}(f_{j+1}^N)$ is still conserved over time, i.e. $\mathcal{M}(f_{j+1}^N) = \mathcal{M}(f_j^N)$. In greater detail, let us consider the following conservation properties.

1. **Mass.** Let the mass of the density function f^s for the species s , be defined as

$$M(f^s) := m^s \int_{\Omega} f^s(t, x, v) dx dv.$$

Note that the mass is proportional to the zero-th moment of the distribution function f^s . The mass of the approximate function $f_{j+1}^{s,N} \in V_j^N$ is

$$M(f_{j+1}^{s,N}) = m^s \sum_{n,k} \widehat{C}_{n,k}^{s,j+1} \int_{\Omega} \psi_n^{\alpha_j^s, u_j^s}(v) \eta_k(x) dx dv = L m^s \alpha_j^s \widehat{C}_{0,0}^{s,j+1}. \quad (15)$$

where L is the length of the spatial interval Ω_x . By virtue of equations (7) for $k = n = 0$, it holds

$$M(f_{j+1}^{s,N}) = L m^s \alpha_j^s \widehat{C}_{0,0}^{s,j+1} = L m^s \alpha_j^s \widehat{C}_{0,0}^{s,j} = M(f_j^{s,N}).$$

2. **Momentum.** The total momentum of f is defined as

$$P(f) := \sum_s m^s \int_{\Omega} v f^s(t, x, v) dx dv,$$

and it is therefore proportional to the first moment of the distribution function. The momentum of the approximate solution $f_{j+1}^{s,N} \in V_j^N \times W^N$ is

$$\begin{aligned} P(f_{j+1}^{s,N}) &= m^s \sum_{n,k} \widehat{C}_{n,k}^{s,j+1} \int_{\Omega} v \psi_n^{\alpha_j^s, u_j^s}(v) \eta_k(x) dx dv \\ &= L m^s \alpha_j^s \left(u_j^s \widehat{C}_{0,0}^{s,j+1} + \frac{\alpha_j^s}{\sqrt{2}} \widehat{C}_{1,0}^{s,j+1} \right) = u_j^s M(f_{j+1}^{s,N}) + L m^s \frac{(\alpha_j^s)^2}{\sqrt{2}} \widehat{C}_{1,0}^{s,j+1}, \end{aligned} \quad (16)$$

where we have used the recurrence relation of the Hermite functions

$$v\psi_n^{\alpha,u}(v) = \alpha\sqrt{\frac{n+1}{2}}\psi_{n+1}^{\alpha,u}(v) + \alpha\sqrt{\frac{n}{2}}\psi_{n-1}^{\alpha,u}(v) + u\psi_n^{\alpha,u}(v), \quad \forall n \in \mathbb{N}. \quad (17)$$

Using the Vlasov–Poisson equations (7) for the unknown spectral coefficients results in

$$\begin{aligned} P(f_{j+1}^{s,N}) &= \sum_s u_j^s M(f_{j+1}^{s,N}) + L \sum_s m^s \frac{(\alpha_j^s)^2}{\sqrt{2}} \widehat{C}_{1,0}^{s,j} \\ &\quad + \Delta t_j \sum_s m^s \alpha_j^s \frac{q^s}{m^s} \int_{\Omega_x} \widehat{C}_0^{s,j+1/2}(x) E_{j+1/2}^N(x) dx. \end{aligned}$$

Note that the discrete Poisson equation in (7) can be recast in a semi-discrete form as

$$\partial_x E_{j+1}^N = \sum_s q^s \int_{\Omega_v} f_{j+1}^{s,N}(t, x, v) dv = \sum_s q^s \alpha_j^s \widehat{C}_0^{s,j+1}(x).$$

Hence, for $E_{j+1}^N \in W^N$,

$$\Delta t_j \sum_s \alpha_j^s q^s \int_{\Omega_x} \widehat{C}_0^{s,j+1/2}(x) E_{j+1/2}^N(x) dx = \Delta t_j \int_{\Omega_x} \partial_x E_{j+1/2}^N E_{j+1/2}^N dx = 0,$$

on account of the periodic boundary conditions. Hence, $P(f_{j+1}^{s,N}) = P(f_j^{s,N})$.

3. Total Energy. Let W be the kinetic energy, defined as

$$W(f^s) := \frac{m^s}{2} \int_{\Omega} v^2 f^s(t, x, v) dx dv, \quad \forall s \in \{e, i\}.$$

The kinetic energy associated with the approximate solution $f_{j+1}^{s,N} \in V_j^N \times W^N$ at time t^{j+1} is

$$\begin{aligned} W(f_{j+1}^{s,N}) &:= \frac{1}{2} m^s \sum_{n,k} \widehat{C}_{n,k}^{s,j+1} \int_{\Omega} v^2 \psi_n^{\alpha_j^s, u_j^s}(v) \eta_k(x) dx dv \\ &= \frac{1}{2} L m^s \alpha_j^s \left[\left((u_j^s)^2 + \frac{(\alpha_j^s)^2}{2} \right) \widehat{C}_{0,0}^{s,j+1} + \sqrt{2} u_j^s \alpha_j^s \widehat{C}_{1,0}^{s,j+1} + \frac{(\alpha_j^s)^2}{\sqrt{2}} \widehat{C}_{2,0}^{s,j+1} \right], \end{aligned} \quad (18)$$

where the recurrence relation (17) has been used twice. Deriving in time and using the Vlasov–Poisson equations (7), results in

$$W(f_{j+1}^{s,N}) = W(f_j^{s,N}) + \Delta t_j q^s \alpha_j^s \int_{\Omega_x} \left(\frac{\alpha_j^s}{\sqrt{2}} \widehat{C}_1^{s,j+1/2}(x) + u_j^s \widehat{C}_0^{s,j+1/2}(x) \right) E_{j+1/2}^N(x) dx.$$

The potential energy associated with the discrete electric field is

$$\mathcal{E}_p(E_{j+1}^N) - \mathcal{E}_p(E_j^N) = \frac{\epsilon_0}{2} \int_{\Omega_x} (E_{j+1}^N(x))^2 dx. \quad (19)$$

To derive a discrete evolution of the potential energy let us first consider the current density

$$J^s(t, x) = q^s \int_{\Omega_v} v f^s(t, x, v) dv.$$

The current density associated with the numerical solution $f_{j+1}^{s,N} \in V_j^N \times W^N$ is

$$J(f_{j+1}^{s,N})(x) = q^s \alpha_j^s \left(u_j^s \widehat{C}_0^{s,j+1}(x) + \frac{\alpha_j^s}{\sqrt{2}} \widehat{C}_1^{s,j+1}(x) \right).$$

The variation of the potential energy reads

$$\begin{aligned}\mathcal{E}_p(E_{j+1}^N) - \mathcal{E}_p(E_j^N) &= \frac{\epsilon_0}{2} \int_{\Omega_x} (E_{j+1}^N(x))^2 dx - \frac{\epsilon_0}{2} \int_{\Omega_x} (E_j^N(x))^2 dx \\ &= \epsilon_0 \int_{\Omega_x} (E_{j+1}^N(x) - E_j^N(x)) E_{j+1/2}^N(x) dx.\end{aligned}\tag{20}$$

Using the midpoint rule for the temporal discretization of Ampère's equation

$$\epsilon_0 \partial_t E + \sum_s J^s(t, x) = 0,$$

and substituting in (20) we obtain

$$\begin{aligned}\mathcal{E}_p(E_{j+1}^N) - \mathcal{E}_p(E_j^N) &= \epsilon_0 \int_{\Omega_x} (E_{j+1}^N(x) - E_j^N(x)) E_{j+1/2}^N(x) dx \\ &= -\Delta t_j \sum_s q^s \alpha_j^s \int_{\Omega_x} \left(u_j^s \widehat{C}_0^{s,j+1/2}(x) + \frac{\alpha_j^s}{\sqrt{2}} \widehat{C}_1^{s,j+1/2}(x) \right) E_{j+1/2}^N(x) dx.\end{aligned}$$

Hence, it can be inferred that the total energy is conserved in the discrete problem, namely

$$\sum_s (W(f_{j+1}^{s,N}) - W(f_j^{s,N})) + \mathcal{E}_p(E_{j+1}^N) - \mathcal{E}_p(E_j^N) = 0.$$

As a second step, we show that the operator from Definition 1 preserves the invariants of the system.

Proposition 4.1. *Let \mathcal{P}_j^N be the operator from Definition 1 and let $f^N \in V_{j-1}^N \times W^N$. It holds*

$$\mathcal{M}(\mathcal{P}_j^N f^N) = \mathcal{M}(f^N),$$

where the functional \mathcal{M} is either mass, momentum, kinetic and potential energy as defined in (15), (16), (18), and (19), respectively.

Proof. Let $\{\widehat{C}_{n,k}\}_{n,k}$ denote the spectral coefficients of f^N and let $\{\widehat{P}_{n,k}\}_{n,k}$ be the spectral coefficients of $\mathcal{P}_j^N f^N$. The matrix \mathbb{P}^j defined in (13) can be written in a more compact way as follows. For $n, m \in \Lambda_{N_v}$ fixed, with $n \geq m$, let us defined $\Lambda_j^{n,m} \subset \mathbb{N}$ as the set of numbers $\ell \in [m, n] \cap \mathbb{N}$ such that $\ell - m$ is even and

$$\ell = \begin{cases} n, & \text{if } u_{j-1} = u_j, \\ m, & \text{if } \alpha_{j-1} = \alpha_j. \end{cases}$$

Then the entries of \mathbb{P}^j read, (with the convention that $0^0 = 1$),

$$\mathbb{P}_{n,m}^j = K_{n,m} \frac{1}{a^{m+1}} \sum_{\ell \in \Lambda_j^{n,m}} \frac{1}{(n-\ell)! \left(\frac{\ell-m}{2}\right)!} \left(-\frac{2b}{a}\right)^{n-\ell} \left(\frac{1}{a^2} - 1\right)^{\frac{\ell-m}{2}}.$$

Let us consider each conserved quantity at a time. Using the definitions above, we have

- (i) **Mass.** According to (15), the mass of $f^N \in V_{j-1}^N \times W^N$ is $M(f^N) = Lm\alpha_{j-1}\widehat{C}_{0,0}$ and the mass of $\mathcal{P}_j^N f^N \in V_j^N \times W^N$ is $M(\mathcal{P}_j^N f^N) = Lm\alpha_j\widehat{P}_{0,0}$. Using the definition of the spectral coefficients from (12) results in

$$M(\mathcal{P}_j^N f^N) = Lm\alpha_j \sum_{n \in \Lambda_{N_v}} \mathbb{P}_{0,n}^j \widehat{C}_{n,0}.$$

Since the matrix \mathbb{P}^j is lower triangular, $\mathbb{P}_{0,n}^j = 0$ for all $n \neq 0$. Moreover, the definition of $\mathbb{P}_{0,0}^j$ gives,

$$M(\mathcal{P}_j^N f^N) = Lm\alpha_j \mathbb{P}_{0,0}^j \widehat{C}_{0,0} = Lm\alpha_j \frac{\alpha_{j-1}}{\alpha_j} \widehat{C}_{0,0} = M(f^N).\tag{21}$$

(ii) **Momentum.** The total momentum of $f^N \in V_{j-1}^N \times W^N$ is defined as in (16), namely

$$P(f^N) = u_{j-1} M(f^N) + Lm \frac{\alpha_{j-1}^2}{\sqrt{2}} \hat{C}_{1,0}.$$

The total momentum of $\mathcal{P}_j^N f^N \in V_j^N \times W^N$ satisfies

$$P(\mathcal{P}_j^N f^N) = u_j M(\mathcal{P}_j^N f^N) + Lm \frac{\alpha_j^2}{\sqrt{2}} \hat{P}_{1,0} \stackrel{(21)}{=} u_j M(f^N) + Lm \frac{\alpha_j^2}{\sqrt{2}} \sum_{n \leq 1} \mathbb{P}_{1,n}^j \hat{C}_{n,0}.$$

Using the expression for the entries of the tranformation matrix \mathbb{P}^j ,

$$\mathbb{P}_{1,0}^j = -\sqrt{2} \frac{\alpha_{j-1}}{\alpha_j^2} (u_j - u_{j-1}), \quad \mathbb{P}_{n,n}^j = \left(\frac{\alpha_{j-1}}{\alpha_j} \right)^{n+1}, \quad \forall n \in \Lambda_{N_v},$$

we can infer

$$\begin{aligned} P(\mathcal{P}_j^N f^N) &= u_j M(f^N) + Lm \frac{\alpha_j^2}{\sqrt{2}} \left(-\sqrt{2} \frac{\alpha_{j-1}}{\alpha_j^2} (u_j - u_{j-1}) \hat{C}_{0,0} + \left(\frac{\alpha_{j-1}}{\alpha_j} \right)^2 \hat{C}_{1,0} \right) \\ &= u_j M(f^N) - u_j M(f^N) + u_{j-1} M(f^N) + Lm \frac{\alpha_{j-1}^2}{\sqrt{2}} \hat{C}_{1,0} = P(f^N). \end{aligned}$$

(iii) **Energy.** Let us first consider the kinetic energy W defined in (18). For $f^N \in V_{j-1}^N \times W^N$, we have

$$W(f^N) = \frac{1}{2} Lm \alpha_{j-1} \left(\frac{\alpha_{j-1}^2}{\sqrt{2}} \hat{C}_{2,0} + u_{j-1} \alpha_{j-1} \sqrt{2} \hat{C}_{1,0} + \left(u_{j-1}^2 + \frac{\alpha_{j-1}^2}{2} \right) \hat{C}_{0,0} \right).$$

Using the definition of the transformation matrix $\mathbb{P}_{n,m}^j$ for $m \leq n \leq 2$,

$$\mathbb{P}_{2,0}^j = \frac{\sqrt{2}}{2} \frac{\alpha_{j-1}}{\alpha_j} \left(\frac{2(u_j - u_{j-1})^2}{\alpha_j^2} + \frac{\alpha_{j-1}^2}{\alpha_j^2} - 1 \right), \quad \mathbb{P}_{2,1}^j = -2 \frac{\alpha_{j-1}^2}{\alpha_j^3} (u_j - u_{j-1}),$$

the kinetic energy associated with $\mathcal{P}_j^N f^N \in V_j^N \times W^N$, satisfies

$$\begin{aligned} W(\mathcal{P}_j^N f^N) &= \frac{1}{2} Lm \alpha_j \left[\frac{\alpha_j^2}{\sqrt{2}} \sum_{n \leq 2} \mathbb{P}_{2,n}^j \hat{C}_{n,0} + u_j \alpha_j \sqrt{2} \sum_{n \leq 1} \mathbb{P}_{1,n}^j \hat{C}_{n,0} + \left(u_j^2 + \frac{\alpha_j^2}{2} \right) \mathbb{P}_{0,0}^j \hat{C}_{0,0} \right] \\ &= \frac{1}{2} Lm \left[\left(\alpha_{j-1} u_{j-1}^2 + \frac{\alpha_{j-1}^3}{2} \right) \hat{C}_{0,0} + \sqrt{2} \alpha_{j-1}^2 u_{j-1} \hat{C}_{1,0} + \frac{\alpha_{j-1}^3}{\sqrt{2}} \hat{C}_{2,0} \right] = W(f^N). \end{aligned}$$

If $E^N \in W^N$ is the electric field associated with the function $f^N \in V_{j-1}^N \times W^N$ via (1), the potential energy (19) reads

$$\mathcal{E}_p(E^N) = \frac{\epsilon_0}{2} \int_{\Omega_x} |E^N(t, x)|^2 dx = \frac{\epsilon_0}{2} \sum_{\substack{k \in \Lambda_{N_x} \\ k \neq 0}} |E_k(t)|^2 = \frac{\epsilon_0}{2} \sum_{\substack{k \in \Lambda_{N_x} \\ k \neq 0}} \frac{1}{k^2} |\alpha_{j-1}^e \hat{C}_{0,k}^e - \alpha_{j-1}^i \hat{C}_{0,k}^i|^2.$$

Since the operator \mathcal{P}_j^N is independent of the Fourier space and the potential energy involves only the first Hermite mode, the conservation follows. In details, $\hat{P}_{0,k}^s = \mathbb{P}_{0,0}^{j,s} \hat{C}_{0,k}^s$ for all $s \in \{e, i\}$ and $k \in \Lambda_{N_x}$. Hence,

$$\begin{aligned} \mathcal{E}_p(\mathcal{P}_j^N f^N) &= \frac{\epsilon_0}{2} \sum_{k \in \Lambda_{N_x}} \frac{1}{k^2} |\alpha_j^e \mathbb{P}_{0,0}^{j,e} \hat{C}_{0,k}^e - \alpha_j^i \mathbb{P}_{0,0}^{j,i} \hat{C}_{0,k}^i|^2 \\ &= \frac{\epsilon_0}{2} \sum_{k \in \Lambda_{N_x}} \frac{1}{k^2} \left| \alpha_j^e \frac{\alpha_{j-1}^e}{\alpha_j^e} \hat{C}_{0,k}^e - \alpha_j^i \frac{\alpha_{j-1}^i}{\alpha_j^i} \hat{C}_{0,k}^i \right|^2 = \mathcal{E}_p(f^N). \end{aligned}$$

□

Note that the conservation properties of the fully discrete adaptive scheme are independent of the choice of the Hermite parameters.

5 Numerical experiments

The implementation of the algorithm for the solution of (7) is the same as for the non-adaptive strategy. We follow Refs. [7, 11, 37] and consider a Jacobian-Free Newton Krylov solver [22] with GMRES for the inner (linear) iterations. Preconditioning strategies which are useful to reduce the number of iterations per time step are discussed in Ref. [11]. Since the change of (u, α) basis is performed at the end of a time step, it amounts to a trivial modification of the implementation of the non-adaptive algorithm.

In order to efficiently update the Hermite parameters and avoid rounding error associated with small variations of the Hermite parameters between two consecutive time steps, we fix two tolerances u_{tol} and α_{tol} . The adaptive Algorithm 1 computes the new Hermite parameters at time t^j based on the strategy described in Section 3.2, but the update is performed only if

$$|u_{j-1}^s - u_j^s| \geq u_{\text{tol}}, \quad \text{and} \quad \frac{|\alpha_{j-1}^s - \alpha_j^s|}{|\alpha_{j-1}^s|} \geq \alpha_{\text{tol}}. \quad (22)$$

If not otherwise specified, the parameters for the nonlinear iterative solver are set as follows: the maximum number of nonlinear iterations is 500; the maximum number of linear iterations is 1000; the maximum error tolerance for residual in the inner iteration is $\eta_{\text{max}} = 0.9$; if not otherwise specified, we take 10^{-9} as absolute and relative error tolerances of the nonlinear iteration.

5.1 Manufactured solution

We begin by using the method of manufactured solutions to study the new algorithm under controlled conditions. Let us consider the domain $\Omega := \Omega_x \times \Omega_v$ with $\Omega_x = [0, 2\pi]$ and $\Omega_v = \mathbb{R}$, and the temporal interval $T = [0, 1]$. Let us assume that the exact solution is given by

$$f^{\text{ex}}(t, x, v) = (2 - \cos(2x - 2\pi t))\pi^{-1/2}e^{-\left(\frac{v-w(t)}{\beta(t)}\right)^2}, \quad (x, v) \in \Omega, \quad t \in T, \quad (23)$$

where $w(t)$ and $\beta(t) \neq 0$ will be specified case by case in our numerical experiments. Assume that $f^e = f^i = f^{\text{ex}}$ from (23) is the exact solution of (1) for all $(x, v) \in \Omega$ and $t \in T$. This entails that $E(t, x) \equiv 0$ for all $x \in \Omega_x$, $t \in T$ if we consider the homogeneous Dirichlet boundary condition $E(t, 0) = 0$ for all $t \in T$. Therefore, f^{ex} in (23) satisfies a simplified Vlasov–Poisson problem, namely the scalar advection problem: For $f_0 := f^{\text{ex}}(0, x, v) \in V|_{t=0}$, and $S \in C^0(T; L^2(\Omega))$, find $f(t, x, v) \in C^1(T; L^2(\Omega)) \cap C^0(T; V)$ such that

$$\begin{aligned} \partial_t f + v \partial_x f &= S, & \text{in } \Omega \times T, \\ f(0, x, v) &= f_0, & \text{in } \Omega. \end{aligned} \quad (24)$$

with

$$\begin{aligned} S(t, x, v) &:= \partial_t f^{\text{ex}} + v \partial_x f^{\text{ex}} = 2(v - \pi) \sin(2x - 2\pi t) \pi^{-1/2} e^{-\left(\frac{v-w}{\beta}\right)^2} \\ &\quad + 2(2 - \cos(2x - 2\pi t)) \pi^{-1/2} \frac{v-w}{\beta} e^{-\left(\frac{v-w}{\beta}\right)^2} \left(\frac{d_t w}{\beta} + \frac{v-w}{\beta} \frac{d_t \beta}{\beta} \right), \end{aligned} \quad (25)$$

where $d_t w$ and $d_t \beta$ are the time derivative of w and β , respectively. The functions $f^{\text{ex}}(t, \cdot, \cdot)$, $S(t, \cdot, \cdot) \in L^2(\Omega)$ for every $t \in T$, admit the spectral expansion

$$\begin{aligned} f^{\text{ex}}(t, x, v) &= \sum_{n \in \mathbb{N}} \sum_{k \in \mathbb{Z}} C_{n,k}(t) \psi_n^{\beta(t), w(t)}(v) \eta_k(x), \\ S(t, x, v) &= \sum_{n \in \mathbb{N}} \sum_{k \in \mathbb{Z}} R_{n,k}(t) \psi_n^{\beta(t), w(t)}(v) \eta_k(x), \end{aligned} \quad (26)$$

with non-zero coefficients $C_{0,0}(t) = 2$, $C_{0,2}(t) = -e^{-i2\pi t}/2$ and $C_{0,-2}(t) = -e^{i2\pi t}/2$. Similarly, algebraic manipulations of the right hand side (25) using the Hermite recurrence relations yield the following non-zero expansion coefficients,

$$\begin{aligned} R_{0,0}(t) &= 2\frac{d_t\beta}{\beta}, & R_{0,2}(t) &= \left(i\pi - iw - \frac{1}{2}\frac{d_t\beta}{\beta}\right)e^{-i2\pi t}, & R_{0,-2}(t) &= \left(iw - i\pi - \frac{1}{2}\frac{d_t\beta}{\beta}\right)e^{i2\pi t}, \\ R_{1,0}(t) &= 2\sqrt{2}\frac{d_tw}{\beta}, & R_{1,2}(t) &= -\frac{1}{\sqrt{2}}\left(i\beta + \frac{d_tw}{\beta}\right)e^{-i2\pi t}, & R_{1,-2}(t) &= \frac{1}{\sqrt{2}}\left(i\beta - \frac{d_tw}{\beta}\right)e^{i2\pi t}, \\ R_{2,0}(t) &= 2\sqrt{2}\frac{d_t\beta}{\beta}, & R_{2,2}(t) &= -\frac{1}{\sqrt{2}}\frac{d_t\beta}{\beta}e^{-i2\pi t}, & R_{2,-2}(t) &= -\frac{1}{\sqrt{2}}\frac{d_t\beta}{\beta}e^{i2\pi t}. \end{aligned}$$

In other words, f^{ex} and S belong to the approximation spaces $V_{\beta,w}^N = \text{span}(\{\psi_n^{\beta,w}(v)\}_{n \in \Lambda_{N_v}}) \times W^N$, where $N = (N_v, N_x)$, with $N_v = 0$, $N_x = 2$ for f^{ex} and $N_v = 2$, $N_x = 2$ for S .

Let us consider the spectral Galerkin discretization of (24) in $V_{\alpha,u}^N$, where we take $N_v \geq 2$ and $N_x \geq 2$. In particular, by taking $N_x \geq 2$, we ensure that the numerical discretization (5) is not affected by any spatial error but only by an approximation error in velocity and time. Since $S \in V_{\beta,w}^N$, using its spectral representation (26), results in

$$\begin{aligned} (S, (\pi 2^n n!)^{-1/2} H_n(\xi) \eta_{-k}(x))_{L^2(\Omega)} &= \sum_{m \in \Lambda_{N_v}} R_{m,k}(t) \int_{\Omega_v} \psi_m^{\beta,w}(v) \psi_n^{\alpha,u}(v) e^{(\frac{v-u}{\alpha})^2} \frac{\sqrt{\pi}}{\alpha} dv \\ &= \sum_{m \in \Lambda_{N_v}} \mathbb{P}_{n,m} R_{m,k}(t), \end{aligned}$$

where $\mathbb{P} \in \mathbb{R}^{N_v \times N_v}$ is the matrix (13) associated with the operator in Definition 1 from $V_{\beta,w}^N$ onto $V_{\alpha,u}^N$. Since $R_{m,k} \equiv 0$ for all $m \in \Lambda_{N_v} \setminus \{0, 1, 2\}$, the fully discrete approximation (7) of (24), can be recast as,

$$\begin{aligned} \frac{\widehat{C}_{n,k}^{j+1} - \widehat{C}_{n,k}^j}{\Delta t_j} + \sqrt{\frac{n}{2}} \frac{2\pi}{L} ik \alpha_j \widehat{C}_{n-1,k}^{j+1/2} + \frac{2\pi}{L} ik u_j \widehat{C}_{n,k}^{j+1/2} + \sqrt{\frac{n+1}{2}} \frac{2\pi}{L} ik \alpha_j \widehat{C}_{n+1,k}^{j+1/2} = \\ \mathbb{P}_{n,0} R_{0,k}^{j+1/2} + \mathbb{P}_{n,1} R_{1,k}^{j+1/2} + \mathbb{P}_{n,2} R_{2,k}^{j+1/2}, \quad \forall (n, k) \in \Lambda_{N_v} \times \Lambda_{N_x}, j \in \Lambda_{N_t}, \end{aligned} \quad (27)$$

where the right hand side vanishes for any $k \in \Lambda_{N_x} \setminus \{-2, 0, 2\}$. If not otherwise specified, the spectral numerical discretization is performed without the artificial collisional operator ($\nu = 0$).

5.1.1 Test case 1: the exact and numerical solutions belong to the same approximation space; $\beta(t) = 1$, $w(t) = 0$, for any $t \in T$, $\alpha = 1$, $u = 0$.

As a first test case, to benchmark the code, we consider as exact solution the function in (23) with $\beta(t) = 1$ and $w(t) = 0$ for all $t \in T$. We solve the fully-discrete problem (27) with the non-adaptive algorithm. The spectral discretization (27) is performed in the finite-dimensional space $V_{\alpha,u}^N$ with $\alpha = 1 (= \beta)$ and $u = 0 (= w)$. The number of Fourier modes is $N_x = 4$ and the time step is set to $\Delta t = 10^{-2}$. The plot on the left of Figure 3 shows the evolution of the L^2 -error for different number of Hermite modes. One can observe that the approximation error is dominated by the temporal error, and it is independent of the numbers of Hermite modes (see also the plot on the right of Figure 3). This is expected since $\alpha = \beta$, $u = w$ and the exact solution f^{ex} belongs to the finite dimensional space $V_{\beta,w}^{(0,2)}$. On the right of Figure 3, the L^2 -error obtained with $N_v = 16$ Hermite modes and $N_x = 4$ Fourier modes is computed for different time steps. As expected, the convergence rate in time is 2.

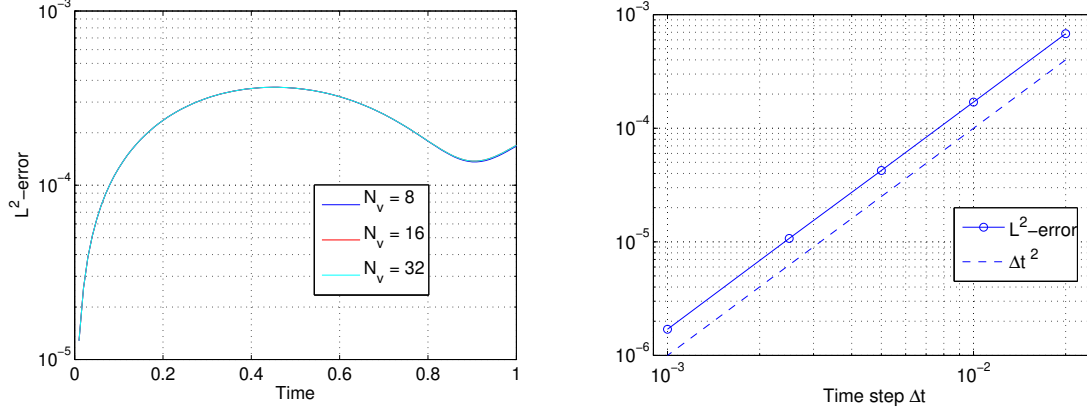


Figure 3: Manufactured solution. Evolution of the L^2 -error for different numbers of Hermite modes (left) with $N_x = 4$ Fourier modes and $\Delta t = 10^{-2}$. L^2 -error vs. time step (right) for $N = (16, 4)$.

5.1.2 Test case 2: the exact and numerical solutions belong to different approximation spaces; $\beta(t) = 1 + t$, $w(t) = 0$, for all $t \in T$, $\alpha = 1$, $u = 0$.

As a second test case we take as exact solution the function f^{ex} from (23) with $\beta(t) = 1 + t$ and $w(t) \equiv 0$. We consider again the non-adaptive algorithm. In order to show that failing to select accurate Hermite parameters, and hence approximation spaces, can have detrimental effects on the numerical solution (cf. Sec. 3), we use a spectral discretization in the finite-dimensional space $V_{\alpha, u}^N$ with constant $\alpha = 1$ and $u = 0$.

Figure 4 (top left) shows the L^2 -error obtained for $\Delta t = 10^{-2}$ with $N_x = 4$ Fourier modes and various N_v , while the evolution of the exact and “approximate” Hermite scaling parameters is presented in Figure 4 (top right). The discrepancy between α and the exact value of β increases linearly over time. In light of this behavior, we can identify three regions in the error evolution (top left plot): (1) at the beginning of the simulation, until around time $t = 0.05$, the accuracy of the simulation is only affected by the temporal error dominating over the error in velocity and all curves for different values of N_v overlap perfectly; (2) then, until around time $t = 0.4$, the error in velocity dominates and increasing the number of Hermite modes is effective in improving the accuracy of the simulation; (3) for $t > 0.45$ the accumulation of error and the lack of accuracy introduced by selecting the wrong Hermite parameters yield to an unstable behavior, as confirmed by the plots of the distribution function Figure 4 (bottom row). One can notice the similarities with the considerations made in Sec. 3.

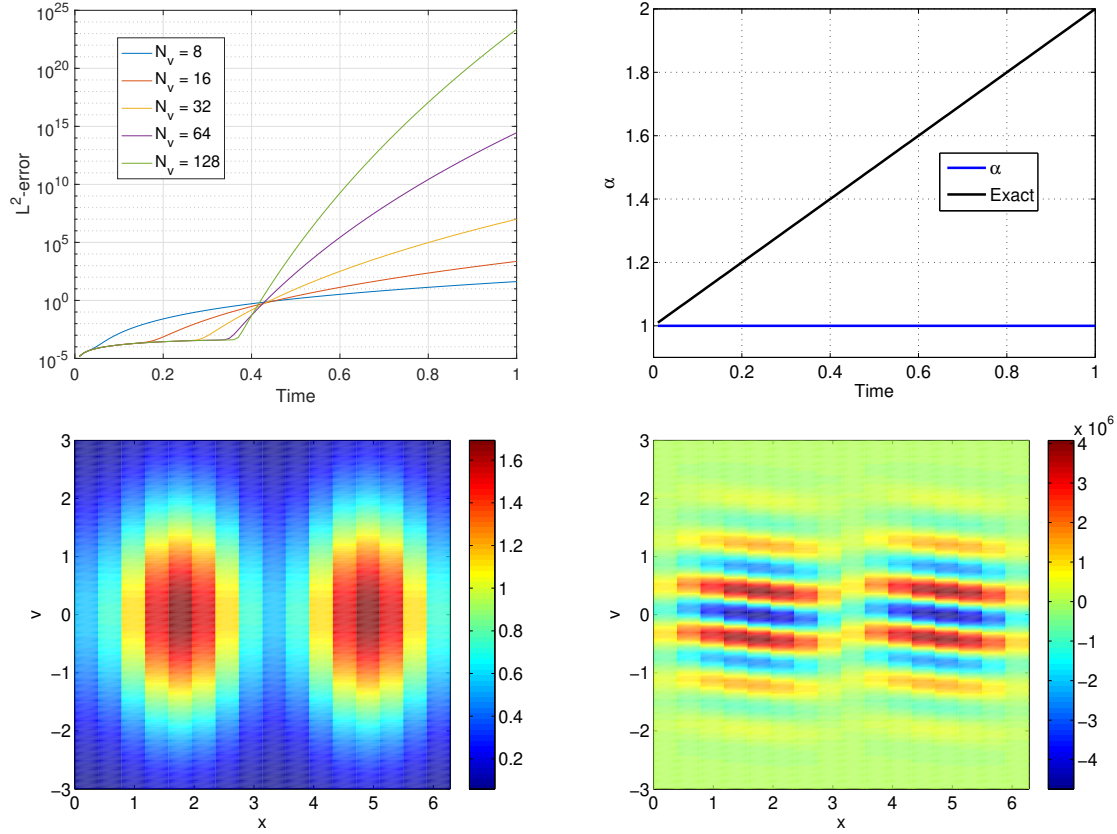


Figure 4: Manufactured solution. Evolution of the L^2 -error for different numbers of Hermite modes (top left) with $N_x = 4$ Fourier modes and $\Delta t = 10^{-2}$. Evolution of β (exact) and α (top right). Bottom row: contour plots of the exact (left) and numerical (right) distribution function at the final time $t = 1$ obtained with $N_x = 16$ Fourier modes and $N_v = 32$ Hermite modes.

5.1.3 Test case 3: $\beta(t) = 1 + t$, $w(t) = 0$, for all $t \in T$, and $\alpha_j = 1 + t^j$, $u_j = 0$ are chosen as piecewise constant approximations of the exact Hermite parameters.

We now repeat the previous test but now the Hermite parameters are selected analytically at each time step, namely $\alpha_j = \beta(t^j)$ and $u_j = w(t^j)$. The results are shown in Figure 5 for $\Delta t \in \{10^{-2}, 10^{-3}\}$. Unlike the previous test, one can notice that the solution converges to the right solution and the L^2 -error is dominated by the approximation in the temporal variable, with a minimal dependence on the number of Hermite modes N_v .

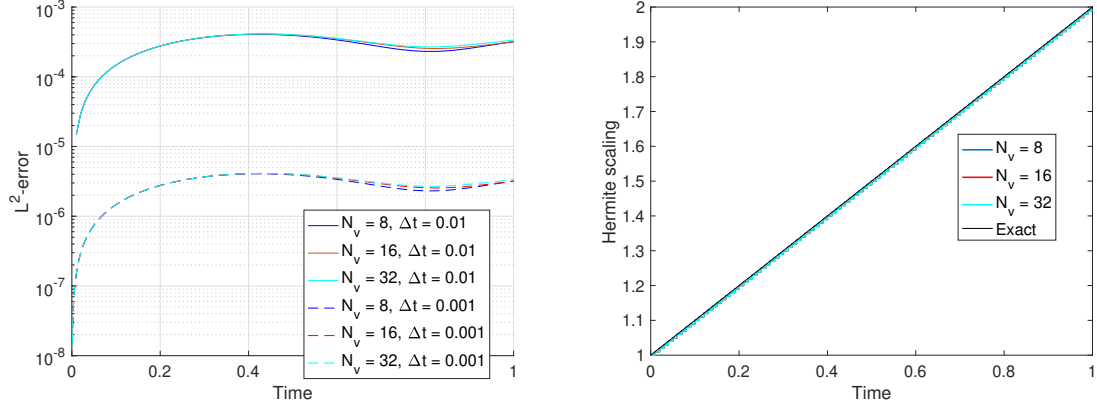


Figure 5: Manufactured solution. Discretization spaces based on the exact values of the Hermite parameters. Evolution of the L^2 -error for different numbers of Hermite modes (left). Evolution of β and α for $\Delta t = 10^{-2}$ (right).

5.1.4 Test case 4: $\beta(t) = 1 + t$, $w(t) = 0$, for all $t \in T$, while α_j and u_j are chosen according to the physics-based criterion.

In the same setting as the previous numerical test, we now consider a spectral discretization in each time interval T_j with finite-dimensional spaces V_j^N where the Hermite parameters are adapted using Algorithm 1 and the physics-based criterion of Section 3.2. The L^2 -error for different numbers of Hermite modes and time steps is shown in Figure 6 (left). On the right plot of Figure 6, the evolution of the Hermite scaling parameter α is presented for different values of N_v . One can notice that the results are practically indistinguishable from those in Figure 5, proving that the physics-based algorithm can track the correct Hermite parameters effectively.

Similar results are obtained with the physics-based adaptive algorithm when also the shifting parameter is changing in time and are not reported for brevity.

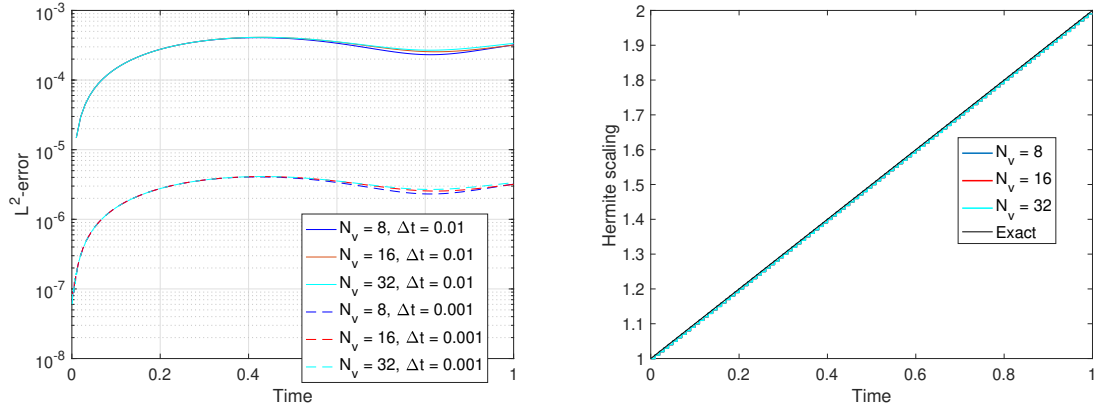


Figure 6: Manufactured solution. Physics-based adaptivity of the Hermite basis functions. Evolution of the L^2 -error for different numbers of Hermite modes (left). Evolution of $\beta = 1 + t$ and α for $\Delta t = 10^{-2}$ (right). The Hermite shift is constant over time, $w = 0$.

In summary, the results shown in this subsection demonstrate the importance of choosing the correct approximation space. In the examples considered, while being too far off from the correct approximation space triggered some numerical instability, the physics-based algorithm is capable of tracking the correct evolution of the Hermite parameters and maintain an accurate numerical solution.

5.2 Two-stream instability

We now consider the two-stream instability, a classical physics benchmark for kinetic plasma codes. It consists of a linear instability excited by two populations of particles counter-streaming with a sufficiently large relative speed.

The initial configuration consists of two drifting Maxwellian electron populations with equal temperature and a Maxwellian at rest neutralizing ion population

$$\begin{aligned} f_0^e(x, v) &= \frac{n_0^e}{\sqrt{\pi}} \frac{1}{\alpha^e} \left(1 + \frac{\epsilon}{2} \cos\left(\frac{2\pi}{L}x\right) \right) e^{-\xi_e^2}, & \xi_e &:= \frac{v - u^e}{\alpha^e}, \\ f_0^i(x, v) &= \frac{1}{\alpha^i \sqrt{\pi}} e^{-\xi_i^2}, & \xi_i &:= \frac{v - u^i}{\alpha^i}, \end{aligned} \quad (28)$$

with $\epsilon = 10^{-3}$, $n_0^e = (\frac{1}{2}, \frac{1}{2})$ and $\alpha^e = (\frac{1}{2}, \frac{1}{2})$, $u^e = (1, -1)$ and $\alpha^i = \sqrt{2 \frac{m_e}{m_i} \frac{T_i}{T_e}}$, $u^i = 0$. We set $\frac{m_i}{m_e} = 1836$ and $\frac{T_i}{T_e} = 1$. Let us consider the Vlasov–Poisson problem in the computational domain $\Omega_x := [0, L]$, with $L = 2\pi$, and $\Omega_v := \mathbb{R}$. The temporal interval $T := [0, T_f]$ is divided into $N_t = T_f/\Delta t$ subintervals with uniform $\Delta t = 0.05$ and the temporal discretization is performed using the implicit midpoint rule. In the adaptive scheme, we take as tolerances (22) for the Hermite parameters $\alpha_{\text{tol}} = 10^{-1}$ and $u_{\text{tol}} = 10^{-2}$.

5.2.1 Comparison for fixed number of Hermite modes and fixed ν

As a first numerical test, let us consider the temporal interval $T = [0, 100]$, and the spectral discretization (5) with $2N_x + 1 = 101$ Fourier modes and $N_v = 250$ Hermite modes. The collisional coefficient of the operator (8) is set to $\nu = 5$.

As is well known, the instability associated with two counter-propagating beams of particles with equal charge proceeds with the development of particle bunching and trapping and the creation of a vortex in phase space. As a result, the drift velocity of each beam decreases while the width of each beam particle distribution increases. This is evident in Figure 7 which shows the evolution of the distribution function for the adaptive (left) and non-adaptive (right) schemes. The evolution of the Hermite parameters is shown in Figure 8, where we can notice a 15% decrease of the beam drift velocity (for each beam). The α parameter, which is associated with the width of the particle distribution, increases by 60%.

The adaptive scheme performs better than the non-adaptive one, as evident when comparing the plots of the distribution function in Figure 7, where can see that the oscillations of the numerical distribution function are eliminated by the adaptive algorithm. Similar considerations can be drawn from Fig. 9 (left), which shows the time evolution of the minimum and maximum values of the distribution function in the phase space domain. In collisionless plasmas, the maximum and minimum values of the distribution function are conserved and therefore monitoring these quantities provides a measure of accuracy of the overall numerical scheme. One can see that the non-adaptive algorithm has large oscillations of both values while in the adaptive algorithm both quantities are preserved quite well: the maximum of the distribution function changes slightly, with relative error smaller than 5% over the whole time interval, while the minimum becomes slightly negative at the end of the simulation but with error (relative to the peak value of the distribution function) less than 3%.

Figure 9 (right) reports the evolution of the error in the conserved quantities momentum and energy, evaluated at the approximate solution with respect to the initial condition. Note that conservation of mass is not shown in the figure since its error is exactly zero. As expected, the conservation laws of momentum and energy are satisfied up to the tolerance of the nonlinear solver [11].

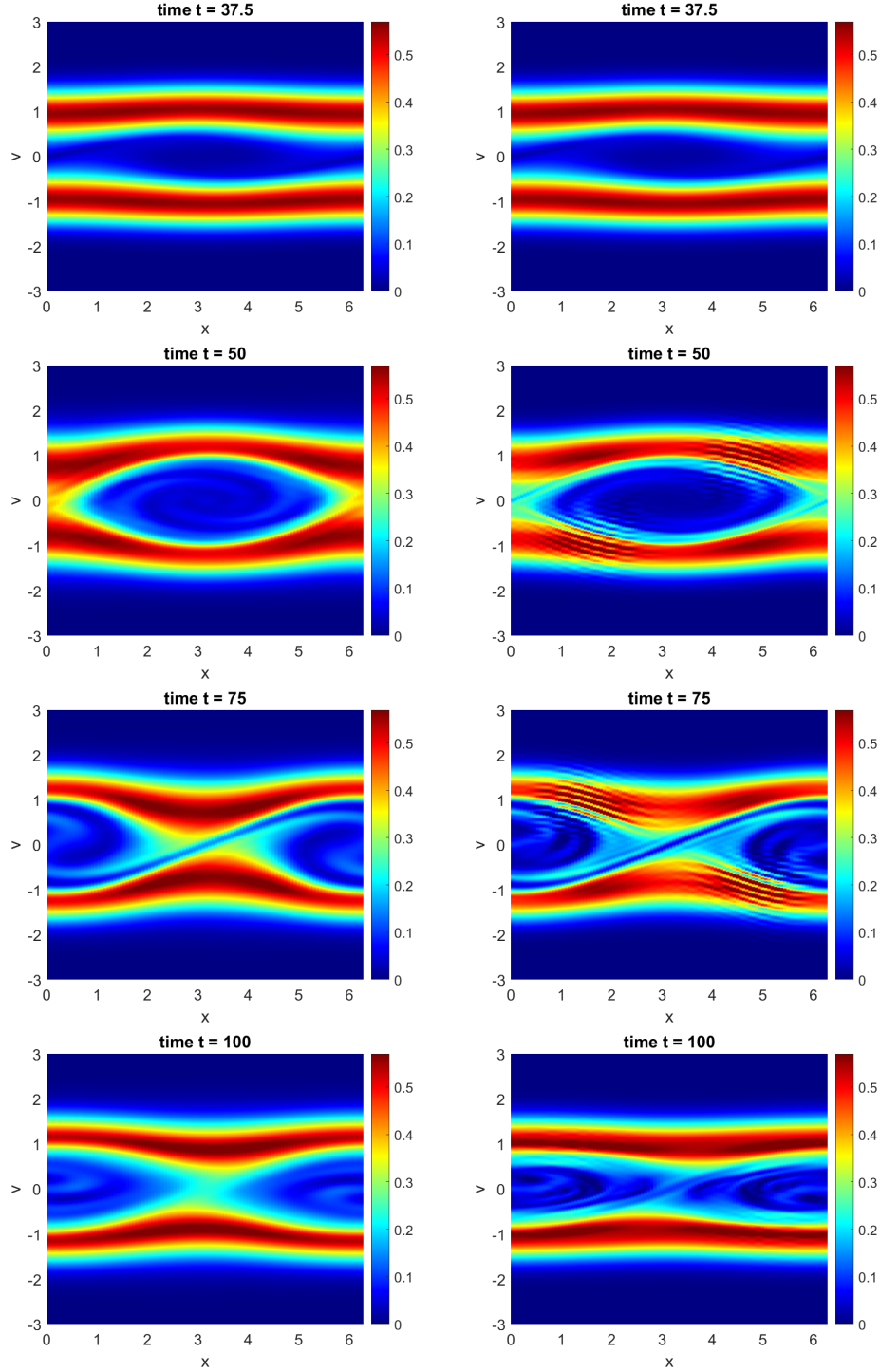


Figure 7: Two-stream instability. Distribution function at different times obtained with the adaptive (left column) and non-adaptive (right column) schemes. The number of Hermite modes is $N_v = 250$, the number of Fourier modes is $N_x = 50$ and the collisional coefficient is $\nu = 5$.

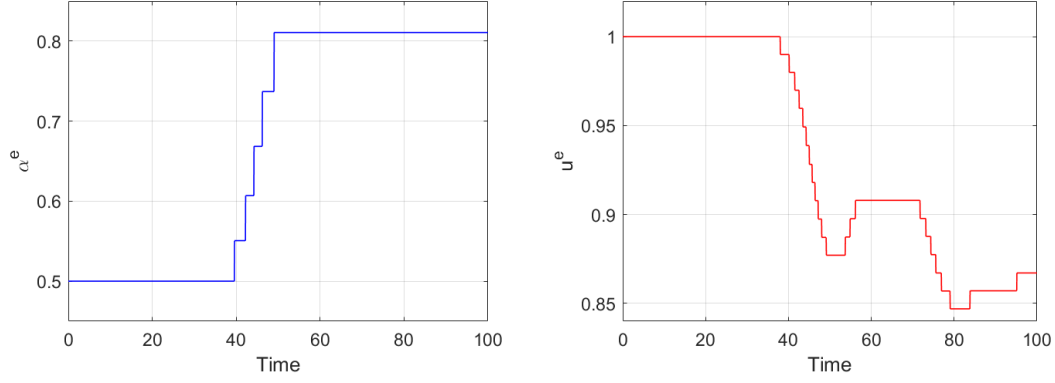


Figure 8: Two-stream instability. Evolution of the physics-based Hermite coefficients. Hermite scaling for electrons α^e (left) and Hermite shift for electrons u^e (right).

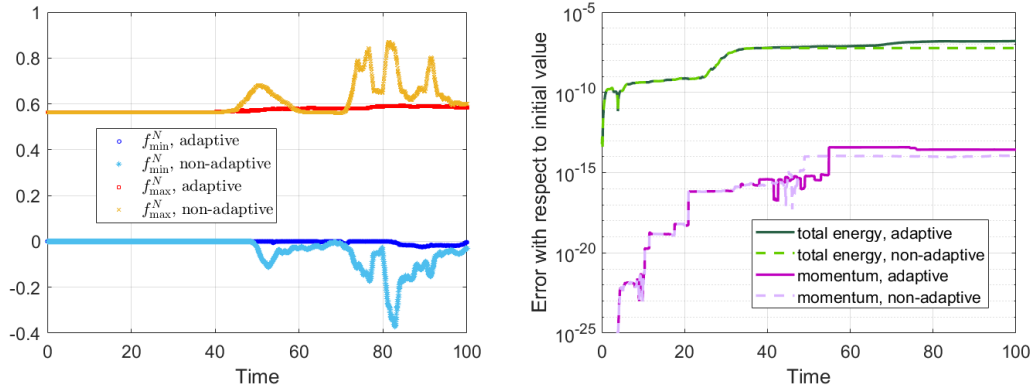


Figure 9: On the left, evolution of the maximum and minimum values of the distribution function for the electron species in the bounded domain $\Omega = [0, L] \times [-3, 3]$ (400 points are used to reconstruct the distribution function in the velocity domain). On the right, numerical verification of the conservation of momentum and energy. The line corresponding to the mass is not shown since the error is exactly zero at all times.

Interestingly, the differences between the two algorithms are not significant when looking at a macroscopic quantity such as the electric field shown in Figure 10. This is likely due to the fact that only one mode is linearly unstable for the parameters considered and this mode, whose linear behavior is captured well by both algorithms, dominates the evolution of the electric field.

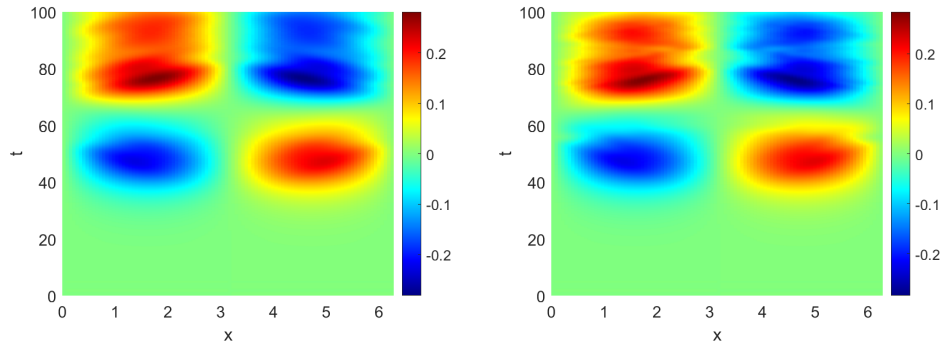


Figure 10: Two-stream instability. Electric field in space and time obtained with the adaptive (left) and non-adaptive (right) schemes.

5.2.2 Comparison with different number of Hermite modes and ν fixed

Let us now consider the temporal interval $T = [0, 50]$, and the spectral discretization (5) with $2N_x + 1 = 101$ Fourier modes. We let the number of Hermite modes vary. The collisional coefficient of the operator (8) is set to $\nu = 5$.

Figure 11 shows that the Hermite scaling α^e evolves in basically the same way for any value of the number N_v of spectral modes. This suggests that the behavior of the Hermite scaling parameter is dominated by the macroscopic behavior of the system, at least in this numerical test.

Figure 12 shows the distribution function at the end of the simulations and the time history of the electric field versus the number of Hermite modes, for both adaptive (first two columns) and non-adaptive algorithms (last two columns). One can notice that the adaptive algorithm is not accurate when $N_v = 10$, while its solutions are visually indistinguishable for all other values of N_v in the range 50 to 250. Conversely, the non-adaptive algorithm shows oscillations of the distribution function throughout the range of N_v considered. These considerations are confirmed in Table 1 showing the minimum and maximum values of the distribution function versus number of Hermite modes. For the parameters considered here, the maximum value of the electron distribution function is 0.56 [Eq. (28)]. For the adaptive algorithm, the minimum of the distribution function on the domain considered, although taking negative values, rapidly converges to zero as N_v increases (polynomial rate of convergence of around 5 for $N_v > 50$). The maximum value of the distribution function is quite well conserved for all cases except $N_v = 10$, with a relative error of only 2% for $N_v = 50$ and further decreasing for larger values of N_v . The non-adaptive algorithm, on the other hand, shows a strong lack of positivity for the lower values of N_v and a slow decay to zero as N_v increases. For $N_v = 250$, however, the relative error on the maximum values of the distribution function remains high, $\sim 21\%$. Generally speaking, the trends of the maximum value of the distribution function in Table 1 show a slow convergence of the non-adaptive algorithm with the number of Hermite modes N_v . Finally, similar to the results shown in Sect. 5.2.1, the behavior of the electric field does not seem to be much affected by the oscillations of the distribution function and the two algorithms produce very similar results.

	$f_{\min}^N(t = 50)$		$f_{\max}^N(t = 50)$	
	non-adaptive	adaptive	non-adaptive	adaptive
$N_v = 10$	-0.8767	-0.0056	0.8837	0.4709
$N_v = 50$	-0.4273	-0.0776	0.6742	0.5836
$N_v = 100$	-0.1383	-0.0275	0.7535	0.5799
$N_v = 125$	-0.0780	-0.0072	0.7246	0.5805
$N_v = 250$	-0.0227	$-3.28 \cdot 10^{-4}$	0.6982	0.5733

Table 1: Maximum and minimum values of the distribution function for the electron species in the bounded domain $\Omega = [0, L] \times [-3, 3]$ for different numbers of Hermite modes.

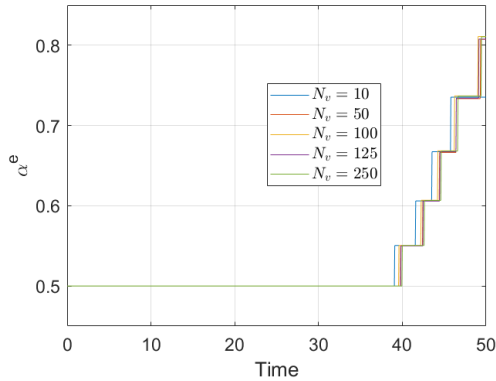


Figure 11: Two-stream instability. Evolution of α^e for number of Hermite modes $N_v \in \{10, 50, 125, 250\}$.

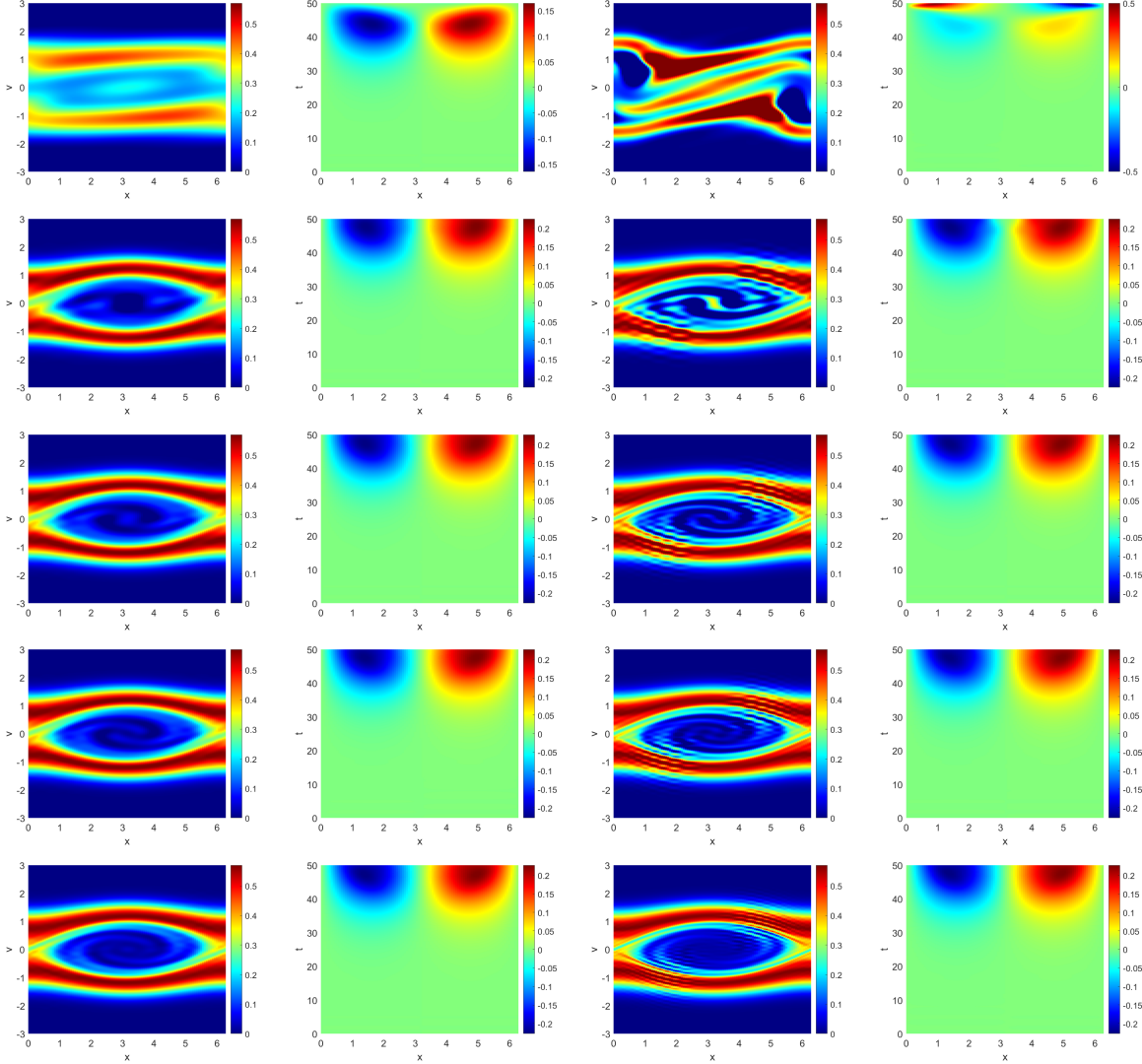


Figure 12: Two-stream instability. First and third columns: distribution function at time $t = 50$ obtained with the adaptive (first column) and non-adaptive (third column) schemes. Second and forth columns: electric field in space and time obtained with the adaptive (second column) and non-adaptive (forth column) schemes. The number of Hermite modes, from top to bottom, is $N_v = 10, 50, 100, 125, 250$. The collisional coefficient is $\nu = 5$ and the number of Fourier modes is $N_x = 50$.

In Figure 13 we compare the adaptive and non-adaptive algorithms in terms of relative error versus a reference solution computed separately, as done for instance in [7]. The reference solution is obtained with the non-adaptive algorithm with $N_x = 50$, $N_v = 1000$, $\Delta t = 0.01$, and $\nu = 10$. Figure 13 (left) shows the L_2 norm of the relative error as a function of time and for different values of the number of Hermite modes N_v . The solid (dashed) lines are for the non-adaptive (adaptive) method. A couple of considerations can be made. First, as the two-stream instability grows and structures develop in the electron distribution function, the error grows in time in both approaches. Second, the error is essentially the same in the early part of the simulation for both approaches. This corresponds to the linear phase of the instability and reflects the fact that at this stage the u and α parameters have not changed considerably (cf. Figs. 8 and 11). Third, in the final part of the simulation the error in the adaptive method is lower than for the non-adaptive method, reflecting that the change of basis is beneficial in improving the accuracy of the solution. This is consistent with the considerations made above, for instance for Fig. 12. The right panel of Fig. 13 shows the L_2 norm of the relative error at $t = 50$ as a function of the number

of Hermite modes N_v , for both adaptive and non-adaptive methods. While the error decreases with increasing velocity space resolution for both methods, it is evident that the adaptive method is more accurate. It also appears to have a faster asymptotic convergence rate than the non-adaptive method.

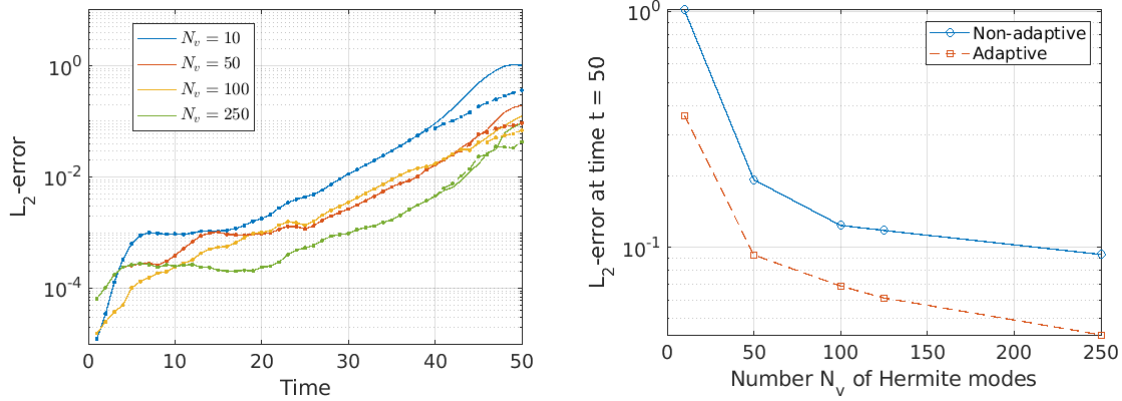


Figure 13: Two-stream instability. On the left, evolution of the L_2 -error between the numerical solution and the reference solution for different numbers of Hermite modes. On the right, L_2 -error at time $t = 50$ vs. number of Hermite modes.

5.2.3 Comparison for different values of ν , for fixed number of Hermite modes $N_v = 100$.

In this Section, we study numerically the interplay between adaptivity and artificial collisionality. We consider the temporal interval $T = [0, 50]$ with $\Delta t = 0.05$. The spectral discretization (5) of the Vlasov–Poisson problem has $2N_x + 1 = 101$ Fourier modes, and $N_v = 100$ Hermite modes. The tolerances for the Hermite parameters are set to $\alpha_{\text{tol}} = 10^{-1}$ and $u_{\text{tol}} = 10^{-2}$.

In Figure 14, we show the distribution function for the electron species at time $t = 50$ for different values of the collisional coefficient ν . For any fixed value of ν , the adaptive schemes gives better results in term of stability and accuracy. On the other hand, as the value of ν increases, filamentation effects are mitigated in both methods (as expected, see also Section 2.2) but the non-adaptive method requires comparatively larger values of ν .

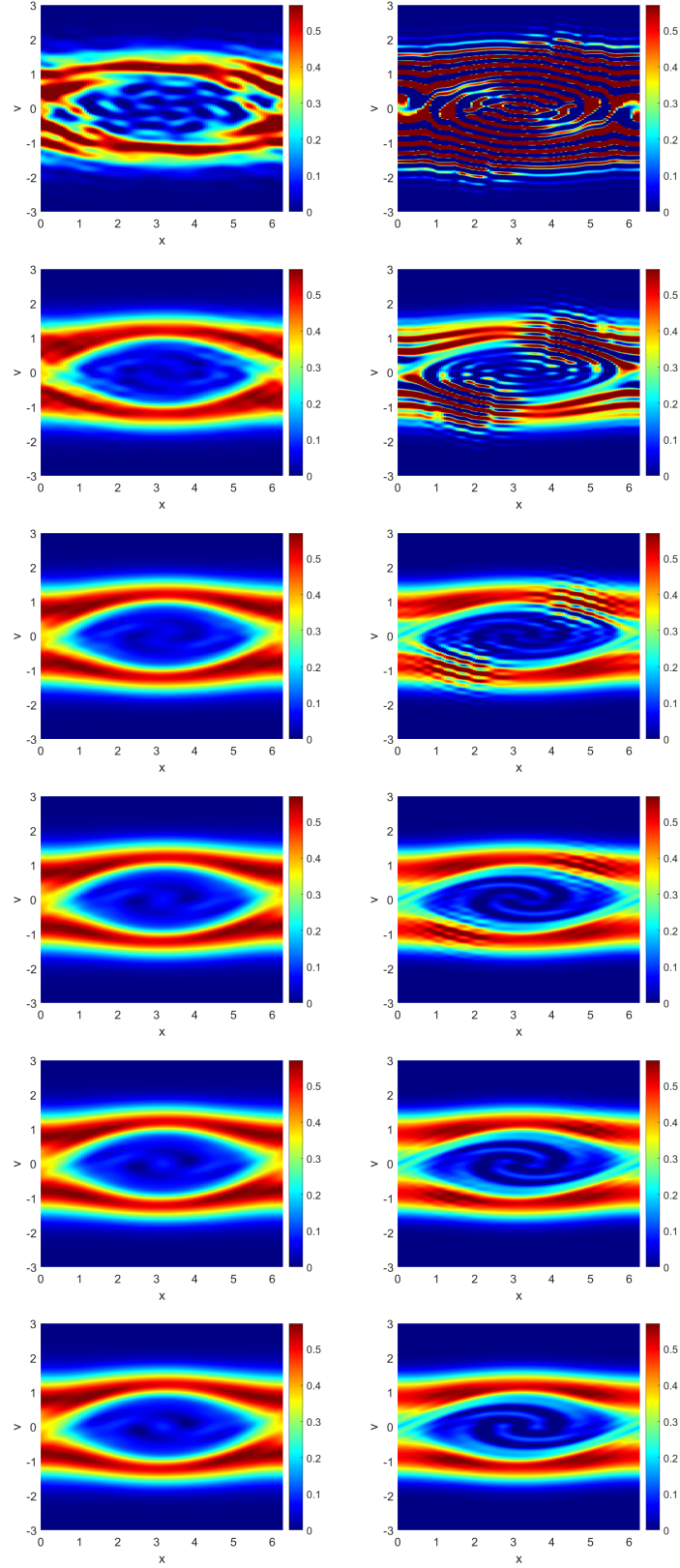


Figure 14: Two-stream instability. Distribution function at time $t = 50$ obtained with the adaptive (first column) and non-adaptive (second column) schemes. The value of the collisional coefficient ν ranges in the set $\{0, 2, 4, 6, 8, 10\}$ from top to bottom. The number of spectral modes is $(N_v, N_x) = (100, 50)$.

In Table 2 the maximum and minimum values of the distribution function for the electron species in the bounded domain $\Omega := [0, L] \times [-3, 3]$ are reported for different values of the collisional coefficient ν . The adaptive algorithm preserves the maximum value of the distribution function quite accurately, with a relative error smaller than 5% for $\nu \geq 3$. For the non-adaptive algorithm, on the other hand, the maximum value of the distribution function varies wildly, but with a decreasing trend with ν . For $\nu = 5$, the maximum value of the distribution function is 34% higher than the initial value. For higher values of ν , it becomes more accurate and the relative error approaches $\sim 3\%$ for $\nu \geq 10$. For both methods the minimum value of the distribution function is negative across all values of ν considered but the adaptive methods performs significantly better.

ν	$f_{\min}^N(t = 50)$		$f_{\max}^N(t = 50)$	
	non-adaptive	adaptive	non-adaptive	adaptive
0	-25.699	-0.3286	25.437	0.9100
1	-7.3866	-0.0743	7.6759	0.6811
2	-2.3657	-0.0368	2.7673	0.6290
3	-0.8270	-0.0206	1.4128	0.6029
4	-0.2777	-0.0208	0.9465	0.5884
5	-0.1383	-0.0275	0.7535	0.5799
6	-0.1067	-0.0350	0.6627	0.5798
7	-0.0973	-0.0400	0.6179	0.5807
8	-0.0930	-0.0433	0.5952	0.5813
9	-0.0994	-0.0454	0.5841	0.5818
10	-0.1088	-0.0459	0.5803	0.5823
11	-0.1219	-0.0454	0.5784	0.5826
12	-0.1338	-0.0438	0.5776	0.5829
13	-0.1495	-0.0426	0.5773	0.5831

Table 2: Maximum and minimum values of the distribution function for the electron species in the bounded domain $\Omega = [0, L] \times [-3, 3]$ for different values of the collisional coefficient ν .

The evolution of the Hermite parameters (not shown) is basically independent of the amplitude of the collisional term, confirming that it is affected predominantly by the macroscopic behavior of the numerical solution and not so much by the higher order Hermite modes which are damped more heavily by the specific form of the collisional operator chosen.

In Figure 15 the electric field is plotted on the spatial domain Ω_x at time $t = 50$ for different values of ν . The right panel shows that the non-adaptive scheme leads to spurious oscillations of the electric field if the collisional coefficient ν is not large enough. In the adaptive scheme, on the other hand, only the case $\nu = 0$ shows some spurious oscillations. Note that the evolution of the L_2 -norm of the electric field, and in particular its slope, is independent of the collision coefficient ν and the growth rate reproduced in all cases (the corresponding plot is not reported since the results obtained with different values of ν are visually indistinguishable). Overall, by comparing the behavior of the adaptive and non-adaptive schemes, we conclude that the adaptive scheme performs better and requires lower value of the artificial collisionality to remove filamentation.

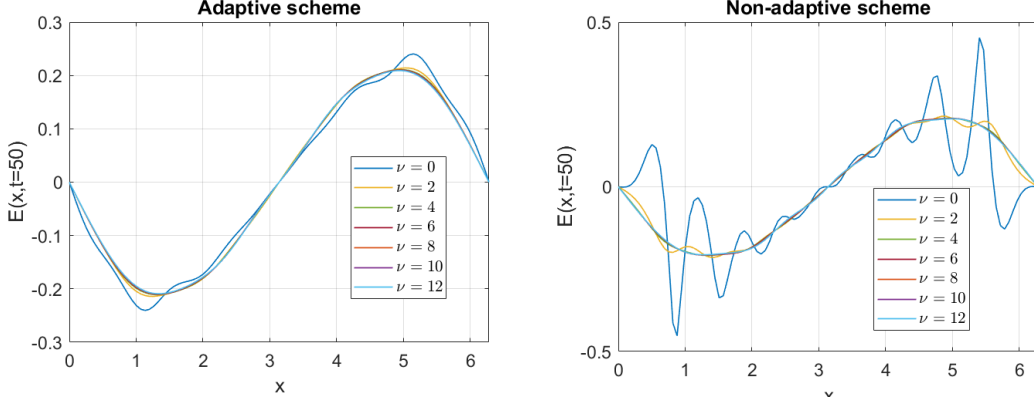


Figure 15: Two-stream instability. Electric field E at time $t = 50$ as a function of the space variable $x \in [0, L]$, for the adaptive (left) and non-adaptive (right) schemes. Different values of the collisional coefficient $\nu \in \{0, 2, 4, 6, 8, 10, 12\}$ are considered.

6 Concluding remarks and outlook

In this work we have presented an adaptive spectral method for the numerical solution of the Vlasov–Poisson equations. The discretization is based on asymmetrically weighted Hermite functions in velocity, and on Fourier basis for the spatial coordinate. Since a poor choice of the basis functions might require spectral expansions with a large number of modes to achieve even moderate accuracy, we have introduced a scaling (α) and shifting (u) of the velocity variable that are adaptively updated in time. The key aspects of the adaptive algorithm are: (i) the mapping between the approximation spaces that are associated with different values of the Hermite parameters α and u ; (ii) the physics-based adaptivity criterion to select and update α and u . The space mapping has been constructed in such a way that adapting the Hermite parameters preserves the total mass, momentum and energy, even in the fully discrete problem, provided that a suitable temporal integrator, e.g. implicit midpoint rule, is used. The strategy to adapt the Hermite parameters is based on physics considerations with the aim of “correcting” the Hermite parameters according to the evolving dynamics. Numerical experiments using both the adaptive and non-adaptive algorithms prove numerically the effectiveness of the new adaptive approach in terms of providing more accuracy and stability of the solution for a fixed level of resolution as well as requiring less numerical viscosity to reduce filamentation effects. The same methodology can be easily extended to the general Vlasov-Maxwell equations.

While spectral methods have emerged recently as potentially attractive methods to study multiscale, micro/macro (fluid-kinetic) coupling problems for plasma physics applications, the adaptivity of the spectral expansion to capture locally the complexity of plasma dynamics and minimize the number of expansion terms needed to achieve sufficient accuracy remains a critical and yet essentially open problem. To the best of our knowledge, the only other approach that involves temporal adaptivity of the spectral expansion for plasma physics applications is the NRxx method of [4] and its recent extension [38]. However, there are substantial differences between our approach and the NRxx method, as highlighted in the introduction.

The only problem-dependent part of the proposed method is the adaptivity criterion: different criteria can be envisioned based on the properties of the dynamics. This could include physics-based criteria like the one proposed in this paper, but also other more mathematical criteria based for instance on the minimization of the error of the numerical scheme via some form of a posteriori error estimation. These could include physics-based criteria like the one proposed in this paper. However, in the presence of non-Maxwellian behavior and highly oscillatory solutions, an adaptivity based on average quantities might not be effective. In such cases, other more mathematical criteria based for instance on the minimization of the error of the numerical scheme via some form of a posteriori error estimation. Extensions of the proposed method to include both spatial and temporal adaptivity of the expansion basis will also need to be developed.

Acknowledgments

The authors acknowledge fruitful discussions with Oleksandr Koshkarov, Gianmarco Manzini and Vadim Roytershteyn. The authors also acknowledge discussions with Juris Vencels in the initial phase of the work. This work was supported by the Laboratory Directed Research and Development Program of Los Alamos National Laboratory under projects number 20170207ER and 20220104DR. Los Alamos National Laboratory is operated by Triad National Security, LLC, for the National Nuclear Security Administration of U.S. Department of Energy (Contract No. 89233218CNA000001). Computational resources for the simulations were provided by the Los Alamos National Laboratory Institutional Computing Program.

References

- [1] T. P. Armstrong, R. C. Harding, G. Knorr, and D. Montgomery. Solution of Vlasov’s equation by transform methods. *Methods in Computational Physics*, 9:29–86, 1970.
- [2] M. Aschwanden. *Physics of the Solar Corona*. Springer Praxis Books. Springer Berlin Heidelberg, 2005.
- [3] R. Bruno and V. Carbone. The Solar Wind as a Turbulence Laboratory. *Living Reviews in Solar Physics*, 2(4), 2005.
- [4] Z. Cai, R. Li, and Y. Wang. Solving vlasov equations using nr\$xx\$ method. *SIAM Journal on Scientific Computing*, 35(6):A2807–A2831, 2013.
- [5] Z. Cai and Y. Wang. Suppression of recurrence in the Hermite-spectral method for transport equations. *SIAM Journal on Numerical Analysis*, 56(5):3144–3168, 2018.
- [6] E. Camporeale, G. L. Delzanno, B. K. Bergen, and J. D. Moulton. On the velocity space discretization for the Vlasov–Poisson system: Comparison between implicit Hermite spectral and Particle-in-Cell methods. *Computer Physics Communications*, 198:47 – 58, 2016.
- [7] E. Camporeale, G. L. Delzanno, B. K. Bergen, and J. D. Moulton. On the velocity space discretization for the Vlasov–Poisson system: Comparison between implicit Hermite spectral and Particle-in-Cell methods. *Computer Physics Communications*, 198:47–58, 2016.
- [8] E. Camporeale, G. L. Delzanno, G. Lapenta, and W. Daughton. New approach for the study of linear Vlasov stability of inhomogeneous systems. *Physics of Plasmas*, 13(9):092110, 2006.
- [9] J. Canosa, J. Gazdag, and J. E. Fromm. The recurrence of the initial state in the numerical solution of the Vlasov equation. *Journal of Computational Physics*, 15(1):34–45, 1974.
- [10] C. Z. Cheng and G. Knorr. The integration of the Vlasov equation in configuration space. *Journal of Computational Physics*, 22(3):330 – 351, 1976.
- [11] G. L. Delzanno. Multi-dimensional, fully-implicit, spectral method for the Vlasov–Maxwell equations with exact conservation laws in discrete form. *Journal of Computational Physics*, 301:338–356, 2015.
- [12] G. L. Delzanno and V. Roytershteyn. High-frequency plasma waves and pitch angle scattering induced by pulsed electron beams. *Journal of Geophysical Research: Space Physics*, 124(9):7543–7552, 2019.
- [13] Y. Di, Y. Fan, Z. Kou, R. Li, and Y. Wang. Filtered hyperbolic moment method for the Vlasov equation. *Journal of Scientific Computing*, 79(2):969–991, 2019.
- [14] F. Engelmann, M. Feix, E. Minardi, and J. Oxenius. Nonlinear effects from Vlasov’s equation. *The Physics of Fluids*, 6(2):266–275, 1963.
- [15] D. Fatone, L. Funaro and G. Manzini. Arbitrary-order time-accurate semi-Lagrangian spectral approximations of the Vlasov–Poisson system. *J. Comput. Phys.*, 384:349–375, 2019.

- [16] L. Fatone, D. Funaro, and G. Manzini. A decision-making machine learning approach in Hermite spectral approximations of partial differential equations. *J. Sci. Comput.*, 92(1):Paper No. 3, 30, 2022.
- [17] H. Gajewski and K. Zacharias. On the convergence of the Fourier-Hermite transformation method for the Vlasov equation with an artificial collision term. *Journal of Mathematical Analysis and Applications*, 61(3):752–773, 1977.
- [18] R. T. Glassey. *The Cauchy problem in kinetic theory*. Society for Industrial and Applied Mathematics (SIAM), Philadelphia, PA, 1996.
- [19] J. P. Holloway. Spectral velocity discretizations for the Vlasov–Maxwell equations. *Transport Theory and Statistical Physics*, 25(1):1–32, 1996.
- [20] V. K. Jordanova, G. L. Delzanno, M. G. Henderson, H. C. Godinez, C. A. Jeffery, E. C. Lawrence, S. K. Morley, J. D. Moulton, L. J. Vernon, J. R. Woodroffe, T. V. Brito, M. A. Engel, C. S. Meierbachtol, D. Svyatsky, Y. Yu, G. Tóth, D. T. Welling, Y. Chen, J. Haiducek, S. Markidis, J. M. Albert, J. Birn, M. H. Denton, and R. B. Horne. Specification of the near-Earth space environment with SHIELDS. *Journal of Atmospheric and Solar-Terrestrial Physics*, 2017.
- [21] G. Joyce, G. Knorr, and H. K. Meier. Numerical integration methods of the Vlasov equation. *Journal of Computational Physics*, 8(1):53 – 63, 1971.
- [22] C. T. Kelley. *Iterative Methods for Linear and Nonlinear Equations*. SIAM, Philadelphia, 1995.
- [23] A. J. Klimas. A numerical method based on the Fourier-Fourier transform approach for modeling 1-d electron plasma evolution. *Journal of Computational Physics*, 50(2):270 – 306, 1983.
- [24] K. Kormann and A. Yurova. A generalized Fourier-Hermite method for the Vlasov-Poisson system. *BIT*, 61(3):881–909, 2021.
- [25] A. Lenard and I. B. Bernstein. Plasma oscillations with diffusion in velocity space. *Phys. Rev.*, 112:1456–1459, Dec 1958.
- [26] N. F. Loureiro, W. Dorland, L. Fazendeiro, A. Kanekar, A. Mallet, M. S. Vilelas, and A. Zocco. Viriato: A Fourier-Hermite spectral code for strongly magnetized fluid-kinetic plasma dynamics. *Computer Physics Communications*, 206:45 – 63, 2016.
- [27] W. Magnus, F. Oberhettinger, and R. P. Soni. *Formulas and theorems for the special functions of mathematical physics*. Third enlarged edition. Die Grundlehren der mathematischen Wissenschaften, Band 52. Springer-Verlag New York, Inc., New York, 1966.
- [28] G. Manzini, G. L. Delzanno, J. Vencels, and S. Markidis. A Legendre-Fourier spectral method with exact conservation laws for the Vlasov-Poisson system. *Journal of Computational Physics*, 317:82–107, 2016.
- [29] G. Manzini, D. Funaro, and G. L. Delzanno. Convergence of spectral discretizations of the Vlasov-Poisson system. *SIAM J. Numer. Anal.*, 55(5):2312–2335, 2017.
- [30] J. T. Parker and P. J. Dellar. Fourier-Hermite spectral representation for the Vlasov-Poisson system in the weakly collisional limit. *Journal of Plasma Physics*, 81(2):305810203, 2015.
- [31] O. Pezzi, F. Valentini, S. Servidio, E. Camporeale, and P. Veltri. Fourier–Hermite decomposition of the collisional Vlasov–Maxwell system: implications for the velocity-space cascade. *Plasma Physics and Controlled Fusion*, 61(5):054005, 2019.
- [32] G. D. Reeves, H. E. Spence, M. G. Henderson, S. K. Morley, R. H. W. Friedel, H. O. Funsten, D. N. Baker, S. G. Kanekal, J. B. Blake, J. F. Fennell, S. G. Claudepierre, R. M. Thorne, D. L. Turner, C. A. Kletzing, W. S. Kurth, B. A. Larsen, and J. T. Niehof. Electron acceleration in the heart of the Van Allen radiation belts. *Science*, 341(6149):991–994, 2013.

- [33] V. Roytershteyn, S. Boldyrev, G. L. Delzanno, C. H. K. Chen, D. Grošelj, and N. F. Loureiro. Numerical study of inertial kinetic-alfvén turbulence. *The Astrophysical Journal*, 870(2):103, jan 2019.
- [34] J. W. Schumer and J. P. Holloway. Vlasov simulations using velocity-scaled Hermite representations. *Journal of Computational Physics*, 144(2):626 – 661, 1998.
- [35] T.H. Stix. *Waves in Plasmas*. American Inst. of Physics, 1992.
- [36] J. Vencels, G. L. Delzanno, A. Johnson, I. B. Peng, E. Laure, and S. Markidis. Spectral solver for multi-scale plasma physics simulations with dynamically adaptive number of moments. *Procedia Computer Science*, 51:1148 – 1157, 2015. International Conference On Computational Science, ICCS 2015.
- [37] J. Vencels, G. L. Delzanno, G. Manzini, S. Markidis, I. B. Peng, and V. Roytershteyn. SpectralPlasmaSolver: a spectral code for multiscale simulations of collisionless, magnetized plasmas. *Journal of Physics: Conference Series*, 719(1):012022, 2016.
- [38] T. Yin, X. Zhong, and Y. Wang. Highly efficient energy-conserving moment method for the multi-dimensional Vlasov-Maxwell system. <https://arxiv.org/abs/2205.12907>, 2022.